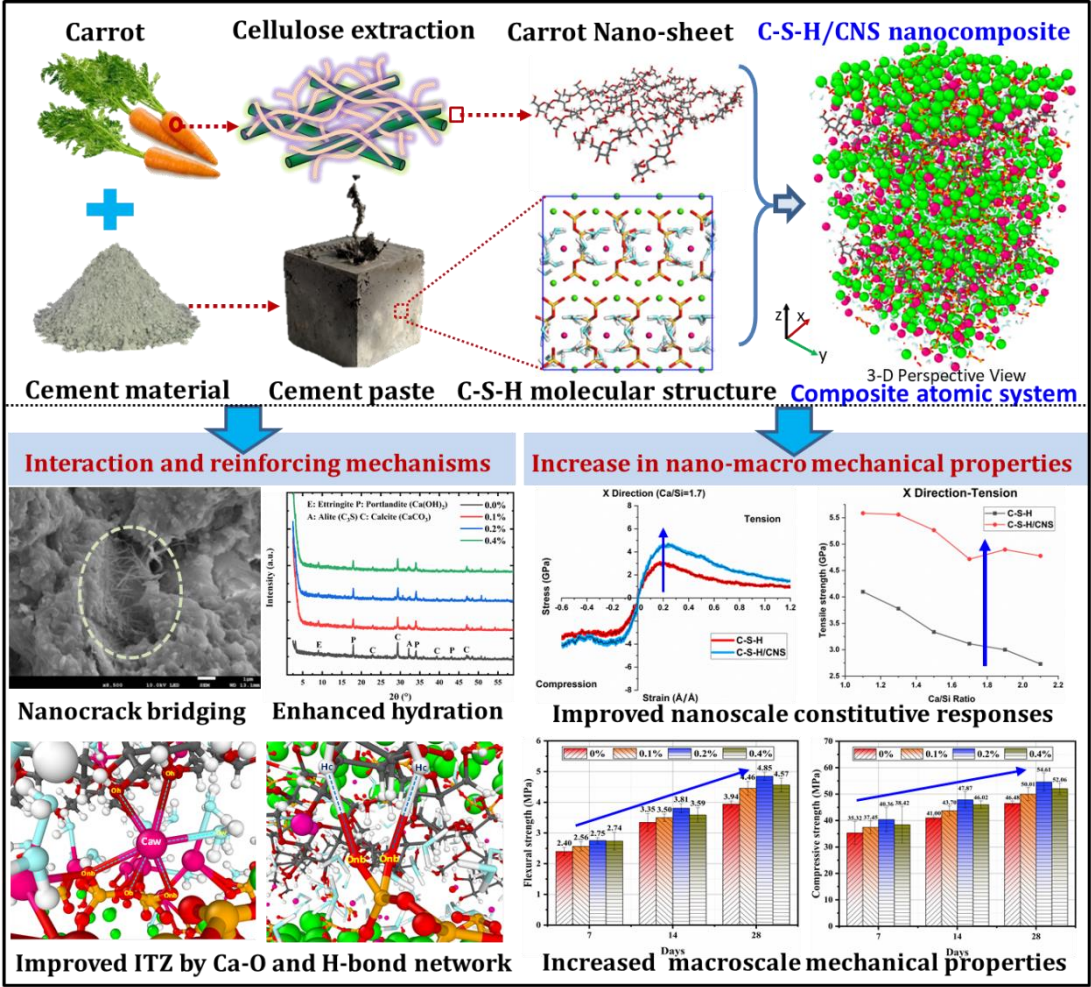


Graphic abstract



Carrot-based covalently bonded saccharides as a new 2D material for healing defective calcium-silicate-hydrate in cement: Integrating atomistic computational simulation with experimental studies

Yin Chi,^{a,b} Bo Huang,^b Mohamed Saafi,^{b*} Jianqiao Ye,^b Colin Lambert^c*

^a School of Civil Engineering, Wuhan University, Wuhan 430072, China

^b Department of Engineering, Lancaster University, Lancashire, LA1 4YW, UK

^c Department of Physics, Lancaster University, Lancashire, LA1 4YB, UK

ABSTRACT:

Concrete is currently produced at a rate of 20 billion tonnes per year and contributes 5-10% of mankind's CO₂ production. If the strength of the calcium-silicate-hydrate (C-S-H), the main binding material of concrete, could be improved, the volume of cementitious material needed for a given structure would be reduced and its environmental impact would be decreased. Here, we show that the constitutive behavior of C-S-H can be improved significantly by complexation with carrot-based cellulose nanosheets (CNSs). This environmentally friendly, reinforcing material heals the defective microstructure of C-S-H, which is responsible for structural deformation and failure at larger length scales. CNSs are built from repeating saccharide units that are covalently linked by a β -1-4 glycosidic (C-O-C) bond. The CNSs show remarkable affinity to C-S-H due to the interfacial Ca-O coordination and H-bond interaction. The functional groups on the surface of the CNS sheet act as a root network, cross-linking the neighboring silicate calcium layers and inhibiting the water dynamics at the silicate nanochannel, thereby significantly improving the interfacial properties of the C-S-H/CNS hybrid structure. The macro experimental results show that the mechanical properties of the composites increase with increasing the concentration of CNSs up to 0.4-wt%. At 28 days and CNS concentration of 0.20-wt%, the flexural strength increases by about 23.2% and the compressive strength increases by about 17.5%. The developed atomic-scale molecular dynamics simulations, combined with top-down experimental measurements of their mechanical properties reveal that the proposed C-S-H/CNS composites

show significant enhancement in strength, stiffness and ductility, and provide a foundation for the development of new high-performance construction materials with lower carbon footprint.

Keywords: calcium silicate hydrate, carrot nanomaterial, molecular dynamics simulation, mechanical properties, cementitious nanocomposites

Correspondence: Prof. M. saafi, E-mail: m.saafi@lancaster.ac.uk, Tel: +44 (0)1524 594070. Dr. Yin Chi, Email: yin.chi@whu.edu.cn, Tel: +86(27)68775337,

1. Introduction

The growing global need for sustainable and environmentally friendly civil infrastructure is driving the development of high-performance construction materials that have high durability and low carbon footprint[1]. Significant past research has been directed at improving the performance of Ordinary Portland Cement (OPC), the most widely used manmade material on earth, by enhancing the nano-micro scale physico-mechanical properties of calcium silicate hydrate (C-S-H), which is the main binder that ‘glues’ the other key ingredients (i.e. sand and gravel) of concrete. For example, nano additives derived from silica aluminate, titanium dioxide and calcium carbonate to mention a few[2–5] were used to accelerate the hydration of OPC and increase the amount of C-S-H which in return improves the bulk properties of the cementitious composites. Novel 1D materials such as carbon nanotubes (CNTs) and 2D materials such as graphene, graphene oxide (GO) and hexagonal boron nitride (h-BN) have been extensively used to create intercalated nanostructures in cement matrix composites (CMCs)[6–13]. The resulting nanoengineered CMCs exhibited improved mechanical performance and durability. Other additives in the form of organic polymers such as poly vinyl alcohol(PVA), poly ethylene glycol (PEG) and poly acrylic acid (PAA) as well as polycarboxylate materials[14–19] were utilized as nano inclusions to improve the fracture energy and toughness of OPC by modifying the microstructure of C-S-H.

Analytical characterization tools coupled with advanced modeling and experimental techniques[20–25] from molecular-scale to macro-scale were used to elucidate the chemical and physio-mechanical properties of these engineered cementitious composites and provide a bottom-up multi-scale composite optimization and damage analysis approach[26–31].

However, the broad industrial application of these nano-modified cementitious composites currently face several hurdles: first, the nanomaterials exhibit poor dispersion capacity in the CMCs as well as tend to agglomerate at high concentrations, leading to the formation of unexpected micro defects and nonhomogeneous microstructure development in the composite systems[32]. The use of CNTs, graphene, GO and h-BN as well as the organic polymers are found to lack strong interfacial adhesion with C-S-H, thereby providing limited performance enhancement of cementitious materials. More importantly, current nanomaterials are expensive to produce and require intensive energy during manufacturing processes. They also pose significant environmental, health and safety risks.

Another way to improve the performance of OPC composites is to reduce defects in C-S-H resulting from a very high calcium-silicate ratio (Ca/Si)[23,33]. Qomi et al.[34] and Pellenq et al.[35] used molecular dynamics (MD) simulations to show that reducing the Ca/Si ratio of C-S-H from 2.1 to 1 would significantly increase its stiffness and strength. However, reducing the Ca/Si ratio by tailoring the microstructure and altering the cement chemistry at an atomic scale is challenging and is impractical for large scale applications.

Cellulose-enhanced CMCs have received a great deal of attention as an attractive alternative to CMCs reinforced with CNTs, graphene, GO or h-BN[36–41]. This is because cellulose-based nanomaterials are abundant, environmentally friendly, inexpensive, highly dispersible in concrete and exhibit better affinity to C-S-H due to their oxygen functional groups. Recently, we demonstrated that when added to CMCs, 2D nano-platelets synthesized from sugar-beet root pulp become bound to C-S-H through hydrogen or ionic/covalent bonds thus forming a three-dimensional network[42]. However, the high concentration of hydroxymethyl functional groups in the sugar-beet fructose unit resulted in significant agglomeration of the sheets in the CMC, which led to inefficient healing of the defective C-S-H as witnessed by the reduction in the mechanical properties of the 2D-sugar beetroot sheet-reinforced cementitious composites[42]. The majority of literature focuses on the use of

different experimental and simulation methods to determine the nanoscale properties of 1-D cellulose crystals[43–45] and C-S-H[46–49]. However, to the authors' knowledge, the properties of bio-based 2D-nanomaterials and their interactions with C-S-H have not been investigated, thus delaying their application in cementitious composites.

In this paper, we present a newly developed CMC reinforced with highly water dispersible 2D carrot-based nanosheets (CNSs) synthesized from carrot waste streams. We perform molecular dynamics simulations combined with experimental characterization to elucidate how the CNSs interact with the defective microstructure of C-S-H. Our atomistic modeling provides fundamental understanding of how the C-S-H/CNS complexes are formed at a molecular-level and how they are translated into interfacial bonding and strength in nanostructured hybrid CMCs with different Ca/Si ratios.

2. Materials and method

2.1 Preparation of carrot-based cellulose nanosheets

The CNSs were fabricated from waste biomass by our industrial partner Cellulocomp L.L.C. (UK) following the procedure developed for sugar beetroot sheets as detailed in[42,50]. The fabrication process is shown in Fig.1. In this process, carrot samples were first treated with sodium hydroxide (0.5mol) where the hemicellulose and pectin were extracted from the plant cells. Subsequently, the solution was heated to 90°C for a period of 5 hours and followed by 1 hour homogenization using a rotating mixer with the rate set varying between 11 and 30 m/s. This achieves the separation of the cells along the line of the middle lamella and results in formation of cell sheets. The carrot sheets were separated from the dissolved materials using a filtration process[50]. The final product is a stable CNS suspension solution with 4% CNS solid and 96% water. A commercial nonionic surfactant was also added to the solution to reduce cellulose aggregation thereby allowing CNSs to be readily dispersed in the aqueous

solutions for a long period of time. This as-received CNS suspension was then used as the additive to prepare the cementitious nanocomposites.

2.2 Preparation of cement pastes

The cement pastes were prepared using ordinary Portland cement (OPC) type CEM I 52.5N. A water-to-cement ratio of 0.35 was used and kept constant for all mixes. The as-received CNSs suspension was first added into the required water with superplasticizer, and the resulting aqueous solution was mildly sonicated for 30 min. The obtained suspensions were then blended with cement powder and mixed for 10 min to prepare the cementitious composite mixtures. The pastes were then poured into plastic molds to fabricate the specimens, which were then shaken for 1 min using a vibrating machine. After 24 hours of curing, the specimens were demolded and cured in the laboratory. For each concentration, prisms (40 mm× 40 mm× 160 mm) and cubes (50 mm × 50 mm × 50 mm) were cast and cured in warm water of a temperature of 20°C to testing for mechanical properties.

2.3 Experimental characterization of cement pastes

The effect of the CNS inclusion on the performance of the cementitious composites was examined. A total of 36 (50×50×50 mm) cube samples were tested at 7, 14, and 28 days to determine their compressive strength. The compression tests were performed using an universal servo-controlled testing system (UTM, Instron 8802J5219, 250KN) according to ASTM C-109[51] with a loading rate of 0.5MPa/s. Thirty-six (40×40×160 mm) prisms were also tested under a four-point bending test at 7, 14 and 28 days to determine their flexural strength. The four-point bending tests were carried out using an ASTM Zwick Roell Z020 machine (C090204019, 20KN, Germany) according to ASTM C78[52]. The tests were conducted using a displacement control with a rate of 0.1 mm/min.

Scanning electron microscopy (SEM) fitted with X-ray Energy Dispersive Spectrometer (EDS) (JSM-7800F) in combination with X-ray diffraction (XRD) (Agilent SuperNova) was used to identify the chemical composition and the microstructure of the hardened cement pastes. Fragments of the samples obtained from the mechanical testing were dried in a vacuum oven for 24 hours at 80° C and coated with gold before imaging. The working voltage ranged from 5kV to 15kV. XRD patterns were recorded at a scanning rate of 2°/min from $2\theta=5^\circ$ to 90° with Cu K α radiation ($\lambda = 1.5418 \text{ \AA}$) on Single crystal.

2.4 Computational methodology

The MD simulations were performed using LAMMPS[53]. Graphic processing of the molecular features was achieved by the open visualization tool OVITO[54]. The stable configurations (i.e., bond, angle, dihedral etc.) with minimum energy were attained by relaxing the composite systems at the beginning of the calculations. In these simulations, the non-linear conjugate gradient (CG) algorithm with an energy tolerance of 10^{-6} Kcal/mole and a force tolerance of 10^{-6} Kcal/mole-Angstrom were used in combination with the isothermal-isobaric (NPT) ensemble for 200000 steps at $T=300$ Kelvin without external constraint. The time step was fixed at 0.5 femtosecond, and a built-in Noose-Hoover style thermo/barostatting with a Verlet time-integration scheme was applied throughout the molecular dynamics simulations. Finally, another 1000 picoseconds run was conducted for the results acquisition. The molecular configurational information and atom dynamic properties were collected every 5 picoseconds for the statistical analysis. For uniaxial tensile and compressive tests, the strain rate was set as 0.008 \AA per picosecond and the periodic boundary condition (PBC) was used to simulate the applied load conditions. During deformation in one direction, the pressures at the other two directions were maintained at zero, allowing the

system to relax without external constraint. The stress–strain curves were captured by recording the pressure development along the load direction as a function of the applied strain. The elastic modulus was calculated from the slope of the linear regime of the stress-strain curve.

3. Results and discussions

3.1 Measurements of micro-structural and mechanical properties

The hierarchical structure, molecular model and SEM micrographs showing the morphology of the CNS are depicted in Fig. 2. The CNS is formed from repeating saccharide units that are covalently linked by a β -1-4 glycosidic(C-O-C) bond (Fig. 2a). The water-based CNS suspension (Fig. 2b) was obtained by the chemical process detailed in the experimental section. The chains are stacked tightly during the biosynthesis process, resulting in the formation of semi-crystalline CNS sheets. As shown in Fig. 2b, the resulting CNS sheets are composed of randomly oriented nanofibrils and their glucose units with symmetrical structure at molecular scale contain less hydroxymethyl groups[55,56] in comparison to the sugar-beet fructose unit, enabling more uniformly dispersion throughout the CMCs. The molecular structure of the CNS and the corresponding chemical stoichiometry of one saccharide unit (Fig. 3) are used to perform MD simulations aimed at probing the behavior of the C-S-H/CNS complexes at atomic level. This provides valuable insight into the interaction and reinforcing mechanisms in the C-S-H/CNS composite, and the nanoscale stress-strain response under different uniaxial tension/compression loading scenarios and Ca/Si ratios.

Firstly, XRD was employed to characterize the change in the microstructure and the hydration phases of the CMCs as a result of the addition of CNS sheets. The XRD patterns of the C-S-H/CNS nanocomposites at CNS concentrations of 0.00, 0.10 and 0.20-wt% at 28 days of curing are shown in Fig. 4a. All samples exhibited similar phases, including ettringite, calcium hydroxide Ca(OH)_2 , un-hydrated tricalcium silicate (C_3S) and calcium carbonate (CaCO_3). The C-S-H hydration phases cannot be identified because of their semi-crystalline

nature. However, their improved growth as a result of the addition of CNS can be quantified by examining the change in the detected crystalline phases of the cementitious composites. Based on the XRD results together with the assorted CrysAlisPro software analysis, we quantitatively identified the proportion of the hydration phases. It is found that the quantities of ettringite, $\text{Ca}(\text{OH})_2$ and other crystals increase, while the un-hydrated phases C3S and CaCO_3 diminish due to the addition of CNS. It can be hypothesized that the addition of CNSs can accelerate the hydration process and result in an increase in the formation of these hydration phases and particularly the amplification of C-S-H growth. The authors are currently testing this hypothesis through in depth experiment characterizations (e.g., TGA/XRD techniques[57]) and reactive MD simulations, which will be discussed in a subsequent publication. Here, we conjecture that the high cement alkaline environment (with $\text{pH}=11.7$) rich in Ca^{2+} ions attenuates/dissolves the acid hydroxyl/hydroxymethyl functional groups on the surface of the CNS sheets. This mechanism can occur during the interaction between the cellulose and cement, where the Ca ions react with the dissolved hydroxyl groups to precipitate the formation of $\text{Ca}(\text{OH})_2$ [42]. The dissociation of functional groups from the CNS typically contributes to the concentration of hydroxyl groups in the solution, which may accelerate the hydration process of cement particles.

Fig. 4b shows SEM images of the nanocomposites along with their corresponding EDX spectra and oxygen maps at mass fractions of 0.00 and 0.40-wt% at 28 days. The microstructure of CMC with 0.00-wt% mainly contains un-hydrated cement particles, micro-cracks and $\text{Ca}(\text{OH})_2$, whereas the microstructure of CMC with 0.40-wt% contains dense C-S-H gels with embedded CNSs to form intercalated nanocomposites. From the EDX spectrum, we can see that the addition of the CNSs increases the content of carbon in the cementitious composite. The oxygen map shows that the cementitious composite with CNSs has denser and more uniformly distributed oxygen peaks. This can be attributed to the excellent uniform distribution of the CNSs within the CMCs.

The effects of the CNSs on the flexural and compressive strengths of the cementitious composites at 7, 14 and 28 days are shown in Fig. 4c,d. As depicted, the flexural strengths increase with increasing the concentration of CNSs, reaching an increase of 14.6%, 13.7%, 23.2% respectively at 0.20-wt% due to both the reinforcing effect and the amplification of C-S-H growth resulting from the CNSs. Similar trend is also observed for the compressive strengths where a maximum improvement of about 17.5% at 0.20-wt% is obtained. It indicates that the morphology of the microstructure of the cementitious composites containing CNSs is more effective in resisting tensile stress than compressive stress due to the crack bridging effect of the CNSs. However, the mechanical properties are decreasing when the CNS concentration rises to 0.4-wt% for all the cases. We hypothesize that at a relative higher CNS concentrations (0.4-wt%), stacking of the CNS sheets may occur in the cementitious composite. As a matter of fact, the high cement alkaline environment that is rich in Ca^{2+} ions captures and attenuates the acid hydroxyl/hydroxymethyl functional groups on the surface of the CNS sheets. This increases the hydrophobicity of CNS due to the carbon rich backbone chain, as a consequence, high van der Waals repulsive forces are created thereby allowing the CNS sheets to stack and agglomerate. When high CNS concentrations are present, agglomerations of CNS tend to form and more defects can be formed within the cementitious composites thus deteriorating their mechanical properties as a result.

3.2 Atomistic simulations of C-S-H/CNS microstructure.

On the basis of the knowledge gained from the macroscale experimental results, we performed MD simulations to uncover the interactions and reinforcing mechanisms at atomic-scale in the bilayer C-S-H/CNS structure. Using the tobermorite 11 Å model proposed by Hamid as an atomic structural benchmark[58], we constructed C-S-H substrate and C-S-H/CNS nanocomposite models with six Ca/Si ratios ranging from 1.1-2.1, which cover the typical range known from experimental observations of different C-S-H products. The critical textural information of the constructed C-S-H molecular model, including the mean

chain length (MCL) and $\text{H}_2\text{O}/\text{Si}$ ratio, is shown in Fig. S1 and Table S1 in the supporting information. The SEM images in Fig. 5a,b demonstrate the intercalation of the CNS chains in the basal structure of C-S-H. This can be further confirmed by examining the XRD patterns of the cementitious composites. Fig. 5c shows the zoomed-in XRD patterns from 2.5 to $6^\circ 2\theta$ and reveals that the XRD pattern of the plain cementitious composite shows a hump-like peak around $3^\circ 2\theta$. When the CNSs are present, this peak becomes broader and less intense, indicating the existence of bilayer C-S-H/CNS crystals in the cementitious composites. Based on this behavior, we constructed a molecular model for the C-S-H/CNS nanocomposite as illustrated in Fig. 5d. The manipulation process of the nanocomposite molecular model is given in Fig. S2. The bonded and non-bonded interactions in the molecular system are defined by a combinational set of parameters from both the ClayFF force field[59], and the Consistent Valence Force Field(CVFF)[60]. We used the classic Simple Point Charge (SPC) model for representing the water, hydroxyl and oxygen-oxygen interactions[61]. The nanocomposite systems were then relaxed in order to attain stable and minimum energy configurations. Uniaxial tension and compression tests were subsequently performed along the x -, y - and z -directions.

Taking the C-S-H/CNS nanocomposite with a median Ca/Si ratio of 1.7 as an example, a typical minimized 3D configuration of the C-S-H/CNS nanocomposite after NPT equilibrium (constant atom number, pressure and temperature) is shown in Fig. 6. This shows that each CNS is in close contact with the neighboring calcium silicate sheet and is highly distorted and wrinkled, exhibiting a pronounced surface disturbance. The different functional groups of the CNSs, including the hydroxymethyl group($-\text{CH}_2\text{OH}$), hydroxyl group($-\text{OH}$) and methine group($-\text{H}$), protrude towards the C-S-H surface and point towards the vacancies of the interlayer water nanometer channel. The initial cleaved nano-pore sized vacuum space in C-S-H is completely closed with the original flat CNSs distorting into an amorphous 3-D carbon-oxygen network structure (see Fig. 6a), implying that a strong binding has been

established between the CNS and the C-S-H. From Fig. 6b, there is a sharp peak in the carbon atom density distribution, with only a small overlap with the density profiles of the interlayer calcium (Caw) ions and water hydrogen (Hw) in the C-S-H model. However, the intensity of both the hydrogen atoms bonded to the CNS glucopyranose ring (Hc) and the hydrogen atoms from the hydroxyl/hydroxymethyl functional groups (Ho) show broader distributions than the backbone carbon atoms (Cc), and their profiles have more overlap with that of Caw. The density profile of Hc from the CNS methine group possesses higher peak and covers the same range as that of Ho from both hydroxymethyl/hydroxyl groups, exhibiting similar binding affinity with the calcium silicate sheets. From Fig. 6b, the presence of Hw atoms in the CNS chain backbone region, indicates that the water molecules migrate from the C-S-H gel and penetrate into the CNS molecular structure. This is attributed to the strong hydrophilic characteristics of the CNS. This is significant, because removing water from C-S-H would reduce its brittleness, enhance its ductility and strengthen the C-S-H/CNS interface owing to the increased Ca-O bonds as discussed below[62].

Fig. 6c illustrates the atom density distribution of the oxygen species from both the CNS and the C-S-H. It is noteworthy that apart from the oxygen atoms from the functional groups (Oh), the glycoside linkage oxygen and ring oxygen (backbone oxygen Oc) atoms are barely interacting with the calcium silicate surface. However, these groups actually weaken the electrostatic repulsion between the carbon atoms and the interlayer calcium cations at the silicate surface, thus contributing further to the connectivity of the CNS to C-S-H. Fig. 6c also shows that the Oh and the Ow atoms are located closer to the silicate non-bridging oxygen (Onb). Therefore, the water molecules, Caw cations, the functional groups of the CNS, the bridging silicate tetrahedra are the main atomic interactions at the interfacial transition zone (ITZ).

Fig. 7 depicts the atomic interactions at the C-S-H/CNS interface. The radial distribution function (RDF) patterns between the Caw and different oxygen species at the interlayer region

of C-S-H are depicted in Fig. 7a. The Caw cations in the C-S-H gel play a key role in crosslinking the neighboring calcium silicate sheets and also are responsible for the interfacial strength between the CNS and C-S-H. From Fig. 7a, one can see that the pronounced peaks in the RDF appear at a Ca-O distance around 2.7 Å for all the four Caw-O RDF patterns, indicating the existence of Ca-O ionic bonding network at the C-S-H/CNS interface. The bond length of Caw-Oh has almost the same value as Caw-Onb with relatively lower peak intensity. As expected, the Caw atoms energetically prefer the Oh atom of CNS. The interlayer Caw atoms are also strongly attracted by the backbone Oc and are orderly arranged in the vicinity of the CNS monolayer due to the electronegativity of the Oc atoms. The bond length order of Caw-O in the ITZ region ranks as follows: Onb>Oc>Oh>Ow. Therefore, the non-bonded ionic interaction between Caw and O species are critical in bridging the silicate tetrahedra and the CNS by forming a stable Si-O-Ca-O-C connection network.

The calculated average oxygen coordination number of Caw with a cutoff distance of 3 Å is shown in Fig. 7b. In the pure C-S-H model, the Caw atoms are coordinated to around 4.8 oxygen neighbors according to different surrounding chemical environments. The coordinated oxygen species are composed of 3.1 Onb, 1.4 Ow and 0.3 Ob (the bridging oxygen in pairing silicate tetrahedra). For the bilayer C-S-H/CNS nanocomposite, the Caw atoms are linked to a higher coordination number of 5 adjacent oxygen neighbors, containing two extra oxygen species, i.e., Oh and Oc from the CNS chain. The coordination number of the Caw in the equilibrated nanocomposite involves 3.1 Onb, 1.1 Ow, 0.3 Ob, 0.2 Oc and 0.3 Oh. The change in the coordinated oxygen species also confirms the established strong ionic connection between the C-S-H substrate and the CNS. The presence of the CNS at the silicate channel can increase the distance between Ow and Caw, which is regarded a key reason for the decreased Ow coordination number in the nanocomposite. In addition, the migration of water to the CNS surface due to the CNS hydrophilicity is also considered as an important reason for the Ow coordination reduction. From the inset picture in Fig. 7b, the Ca atoms clustered

with surrounding oxygen atoms having 6- to 7-fold coordination can form disordered octahedrons, leading to a more amorphous interfacial structure and strengthened C-S-H/CNS interface. This was also observed in previous studies[63].

In addition to the Ca-O ionic bond interaction, the hydrogen-bonding are also an important counterpart in crosslinking the C-S-H and the CNS. Fig. 7c shows the RDF patterns between different hydrogen species versus Onb atoms from C-S-H. The first peak in the RDF of Onb-Hw distributing from 1.7 to 2.4 Å, indicates the strong H-bond interaction between the silicate tetrahedral oxygen and surrounding water hydrogen atoms. The Hc atoms also have relative strong correlation with the Onb atoms. The defective silicate chains in the C-S-H offer a great number of non-bridging oxygen sites to accept H-bonds from the abundant methine functional groups of the CNS. The Hc atoms not only donate H-bonds and contribute to the affinity of the CNS to the C-S-H substrate surface, but also improve the interfacial property by forming a Si-O-H-C like connection system that is directly crosslinking the CNS and the C-S-H substrate surface. The representative local H-bond in the ITZ is illustrated in [Fig. 7d-i](#).

In addition, it is noticed from Fig. 7c that the Ho atoms from the hydroxymethyl/hydroxyl functional groups of CNS have peculiar inconspicuous correlation with the non-bridging oxygen. This is attributed to the most of H-bond accepting sites from the silicate chains being occupied by the water molecules that restrict the mobility of the CNS functional groups. The obscure Onb-Ho bond is also due to the constraint of intra- molecular hydrogen bonds within a single CNS chain as well as the inter-molecular hydrogen bonds between the adjacent chains. These inter- and intra- molecular H-bonds within the CNS help maintain its integrity without de-protonation of the functional groups, whose patterns are schematically illustrated in Fig. S3. The RDF pattern shown in [Fig. 7j](#) further confirms the strong spatial correlation between Oc and Ho within the CNS. As can be seen, there is a sharp peak at a short range distance of 2.5 Å, primarily contributed by the O3-HO3...O5

intra-molecular hydrogen bond connection. This connection is highly stable during the deformation, which helps the nanocomposite resist the tensile stress along the chain direction.

Fig. 7k shows that there are strong short-range spatial correlations between oxygen from CNS and the hydrogen from water, as well as the oxygen from water and the hydrogen from the CNS molecular structure. The initial peaks of $O_{\text{CNS}}\text{-}H_{\text{w}}$ are positioned at around 2 Å, and further positions of $O_{\text{w}}\text{-}H_{\text{CNS}}$ are observed, implying that the CNS is more likely to act as H-bond acceptor. The oxygen in the CNS can provide an H-bond accepting site and is prone to connect water hydrogen H_{w} to form an $\text{O}\text{-}H_{\text{w}}\text{-}H_{\text{w}}\text{-}\text{O}$ like linkage. The CNS can also donate H-bonds to the O_{w} mainly via methine groups of CNS, thereby crosslinking the neighboring silicate tetrahedral by $\text{H}\text{-}O_{\text{w}}\text{-}H_{\text{w}}\text{-}\text{O}$ connections. As a consequence, the bulk water in the interlayer region of C-S-H serves as an aqueous medium, connecting the CNS and the C-S-H gel surface by forming inter-molecule H-bond networks.

The H-bond network established between the CNS and the C-S-H are classified as the structural hydrogen-bonding in the nanocomposite, which differ significantly from those among the water molecules[64]. The broader RDF pattern of $O_{\text{w}}\text{-}H_{\text{o}}$ with peak position larger than 2.45 Å confirms that the hydroxyl groups of CNS are primarily gathered around the inter calcium layer at the ITZ region due to the inter- and intra-molecule H-bonds within the chain and are ultra-confined by the surrounding bulk water.

The H-bond network at ITZ can further mitigate the water dynamics at the interlayer nano-channel. The dynamics of the H_{w} atoms in the nanocomposite are characterized by their mean square displacement (MSD). The overall MSD evolutions of different atom chunks as a function of time are shown in Fig. S4. In comparison to the pure C-S-H model, the dynamics of neighboring water molecules are highly restrained for the nanocomposite (Fig. 7l). The translational diffusion coefficients D approximated by linear regression of the MSD curve are summarized in Table S2 for different Ca/Si ratios. The diffusion coefficient of water at the pore surface in the hydrated cement paste is approximate 1/61 of the water bulk and the

corresponding diffusion coefficient in the CNS reinforced C-S-H is much less than that in the plain C-S-H with D values fluctuating around $2.2 \times 10^{-11} \text{m}^2/\text{s}$ for most cases. Because the distorted chain acts as a reservoir and retains the water molecules, the hydroxyl/hydroxymethyl and methine functional groups of CNS that are deeply embedded into the bulk water act like a root network cross-linked to the neighboring silicate calcium layer, which blocks the water channels, thus inhibiting the water movement. It is worth mentioning that the rapid streaming of water in the nano-channel in the C-S-H can produce a strong repulsive force and fluid pressure that disturb the chemical bonds in the C-S-H and weaken the connections between the neighboring calcium silicate layers[65]. Therefore, one significant benefit of using CNS is to stabilize the interlayer water, reduce the flowability of the composite material and strengthen the interfacial connection.

3.3 Atomistic simulations of C-S-H/CNS mechanical behavior

The stress-strain curves of the nanocomposites when they are subjected to uniaxial tension/compression provide insights into the constitutive relationships of the materials at the atomic scale. Taking $\text{Ca/Si}=1.7$ as an example, the plain C-S-H shows distinct anisotropic mechanical behaviors as depicted in Fig. 8a. As shown, when subjected to tension, C-S-H exhibits a ductile behavior in both the x - and y - directions and a brittle behavior in the z -direction. The tensile strength of the C-S-H structure in the x - direction is due to the interaction between the silicate tetrahedra and the calcium clusters. The C-S-H structure in the y - direction provides the highest strength as the long silicate chain growing along the y -direction contributes significantly to the tensile resistance. However, in the z - direction, the presence of water in the C-S-H nano-pore weakens the Ca-O-Si bonding between neighboring calcium silicate layers by isolating the calcium ions from the surrounding oxygen atoms. The segregation generally occurs at this interlayer region during tensile loading, thus showing the lowest tensile strength. For compressive behavior, there are no significant differences among the three directions.

Fig. 8b-d compares the stress-strain curves between the pure C-S-H and the bilayer C-S-H/CNS nanocomposite along the x -, y - and z - directions, respectively. It can be clearly seen that CNS has a significant impact on the mechanical response of C-S-H when subjected to uniaxial tension or compression. A discernible higher stiffness is observed in the elastic stage in the bilayer C-S-H/CNS nanocomposites for all the three directions. This is due to the contribution of the relative high Young's modulus of the CNS crystal (computed as 128GPa in the current work). In addition, the strength and the ductility are increased in both tension and compression.

In the x - direction (Fig. 8b), the reinforcing effect of CNS is significant where the peak stress is increased by approximate 50%. This is because the CNS chain is parallel to the tensile loading direction, thus providing a crack bridging effect in C-S-H, which in return helps transfer the stress between the defective silicates. In addition, the strong C-C covalent bond and the C-O-C glucose linkage within the CNS backbone resist mechanical deformation in the x -direction. For compression, the compressive stress-strain curve of the C-S-H/CNS nanocomposite is similar to that of the plain C-S-H with a moderate increase in the compressive strength up to around 23% for Ca/Si=1.7.

In the y - direction (Fig. 8c), the tensile strength of the C-S-H is increased by approximately 16%, primarily due to the contribution of the inter-molecular H bond connections (O2-HO2...O6) between the adjacent CNS chains. The reinforcing effect of the CNS in the y -direction only exists in the pre-peak region, because the inter-molecular H bond connections between the adjacent chains can be easily ruptured at small deformations. As such, the C-S-H nanocomposite exhibits similar post-peak performance to that of the plain C-S-H gel but with higher stiffness and tensile strength in the pre-peak region. The shape of the compressive stress-strain curve of the C-S-H/CNS nanocomposite is also similar to that of the C-S-H and shows increase in the compressive strength by up to 25%.

In the z - direction (Fig. 8d), the tensile strength of the C-S-H/CNS nanocomposite under

tension is slightly higher than the tensile strength of the plain C-S-H (see Table S3). The insertion of CNS into C-S-H also increases the tensile deformation of the C-S-H/CNS nanocomposite in the post-failure region between 0.1 and 1.0 $\text{\AA}/\text{\AA}$. This means that the inclusion of CNS improves the ductility of the C-S-H along the interlayer direction due to the plasticity feature of CNS. As previously discussed, the presence of CNS provides more Ca-O coordination and donates H-bond to the neighboring calcium silicate layer, thus improving the interfacial bond between the silicate layers. In addition, as the water in the C-S-H layers migrates to CNS, calcium ions that previously shielded by the water molecules are now free to form more amorphous Ca-O connection networks, thereby further strengthening the interface between the silicate layers. This results in an increase in the tensile strength of about 20% (see Fig. 8d and Table S3). The improvement in the compressive behavior of the C-S-H/CNS nanocomposite is much more evident in the z - direction. This is because the CNS monolayer lying in the x - y plane restrains the lateral dilation of the structure. The compressive strength of the C-S-H/CNS nanocomposite is increased by 36% (Fig. 8d and Table S3). The compressive stress-strain response of the C-S-H/CNS nanocomposite is characterized by an apparent strain hardening phenomenon in the post-peak response due to the passive confinement from CNS.

Fig. 8e illustrates the typical evolution of the structural morphology of the C-S-H and C-S-H/CNS nanocomposites under tension in the x - direction with Ca/Si=1.7. The tensile stress-induced damage processes are compared at strain levels of 0.16, 0.48, 0.80, 1.2 $\text{\AA}\text{\AA}^{-1}$.

As shown in Fig. 8e, the pure C-S-H and the bilayer C-S-H/CNS nanocomposites exhibit different damage processes. During tensile loading in the x - direction, as the strain increases, the layered structure of the pure C-S-H is slightly disturbed at the beginning, indicated by rearrangements of the silicate tetrahedral structure. When the strain reaches 0.4 $\text{\AA}\text{\AA}^{-1}$, micro cracks start to nucleate between the silicate layers and then coalesces into a vertical macro crack. This leads the failure of the C-S-H system. For the C-S-H/CNS nanocomposite, the

CNS monolayer remains flat in the interlayer region at all the strain levels. At the beginning of the tensile loading, the carbon-carbon and carbon-oxygen covalent bonds in the CNS chains are elongated together with the C-S-H matrix. As previously mentioned, the interfacial connection between the CNS and the C-S-H substrate is primarily controlled by the Ca-O ionic bonds and H-bonds, which are weaker than the C-O-C glucose bonds as well as C-C and C-O covalent bonds within the CNS. As a result, the CNS chain is gradually pulled out from the interlayer region during the continuous loading process. Even though a large number of functional groups grafted on the CNS surface can provide sufficient oxygen sites and donate H-bonds necessary to adhere to the calcium silicate sheet, the ITZ between the CNS and the C-S-H surface still remains as one of the weakest links in the nanocomposite system. Therefore, as the strain is continuously increased, the ionic bonds are steadily broken and the tensile stresses undertaken by the non-bonded electrostatic interaction are gradually transferred to the CNS chain, resulting in a “friction-like effect” between the CNS chains and the surrounding C-S-H substrate. Consequently, the mechanical behavior in terms of strength and post-peak ductility are dramatically improved. When the strain reaches 1.2 \AA^{-1} , the calcium silicate sheet in the bilayer C-S-H/CNS nanocomposite remains intact and only a nanopore sized vacancy appears after the pullout of the CNS chains. On the other hand, a complete fracture is observed in the pure C-S-H with a huge crack opening at the center. The entire failure processes and the corresponding morphologies and descriptions in the y- and z- directions are illustrated in Fig. S5 and S6, respectively, in the supporting information.

The deformation simulation results at nano-scale provide molecular insights into the interfacial property between the C-S-H and the CNS, which is the origin of enhanced macro mechanical properties observed in our experiments.

During tension, the typical bond length evolutions (BLE) and the bond angle distributions (BAD) for the bilayer C-S-H/CNS nanocomposite with Ca/Si=1.7 is demonstrated by the probability density distribution. The relation between mean bond

length/angle values versus tensile strain are plotted in Fig. 9. Here, we focus on analyzing the C-C and C-O bond in the CNS backbone chain to probe its contribution to the strain evolution in the x - direction. For the y - and the z - directions, the BLE and BAD are shown in Fig. S7 and S8 in the supporting information. Fig. 9a shows the BLE of the C-C bond in the glucopyranose ring from a strain level of 0.04 \AA\AA^{-1} to 0.4 \AA\AA^{-1} in the x - direction. The distributions of the BLE are gradually shifted towards the right with an increase in the strain level, indicating that the lengths of the C-C bonds have been increased during the tensile deformation. The mean C-C bond length is slightly increased from 1.527 \AA to around 1.555 \AA due to the strong covalent bond between the carbon atoms. However, the BLE of the C-O bond is much more significant. As clearly seen from Fig. 9b, the C-O bond length increases steadily from 1.46 \AA to 1.54 \AA , suggesting that the glucose linkage (C1-O1-C4) and the epoxy linkage (C1-O5-C5) are much weaker than the carbon-carbon bond in the CNS. When viewed in conjunction with the corresponding BAD shifts, the reorientation of the CNS structure simultaneously occurs to adapt to the increasing strain, rather than merely bond-stretching. It can be seen from Fig. 9c that the BAD of the C-C-C shows a much broader distribution (from 80 to 140 deg) during the continuous loading with minor variations of the mean bond angles from 104.5 to 106.5 deg . This implies that the glucopyranose ring undergoes in-plane stretching together with a strong distortion of the hexagonal saccharide unit. From the C-O-C linkage shown in Fig. 9d, we can see that the BAD moves significantly towards the right with a significant change in the mean bond angle from 115 to 124 deg . This is responsible for the elongation of the CNS chains. The distortion of the CNS chains and stretching of glycosidic bonds occurring during the early load bearing process contribute to the increase in the nanocomposite stiffness due to the high modulus of CNS.

From Fig. 10, both the mean bond length and the mean bond angle increase proportionally with the strain increment until the structure is stretched to the peak strain level of around 0.2 \AA . Subsequently, a plateau with slight oscillation is observed as the strain

gradually increases. No significant change in bond characteristics occur after the peak strain, confirming that in the x - direction, the CNS maintains its deformed shape and is gradually pulled out from the C-S-H substrate during the tensile loading. This is due to a higher tensile strength of the CNS in the x - direction in comparison to that of the pure C-S-H.

Fig.11 shows the stress-strain responses of the C-S-H and C-S-H/CNS nanocomposite in the x - direction at different Ca/Si ratios. The stress-strain responses of all samples in the x -, y -, z - directions are summarized in Fig. S9 and their maximum tensile and compressive stresses are tabulated in Table S3 in the supporting information. From Fig. 11a, the mechanical properties (i.e., stiffness and tensile and compressive strength) of C-S-H are gradually decreasing with increasing the Ca/Si ratio. A similar trend is also observed in the C-S-H/CNS nanocomposite as shown in Fig. 11b. This is due to the fact that the degree of defectiveness of C-S-H increases with an increase in the Ca/Si ratio, thus resulting in lower mechanical properties.

Fig. 11c,d depicts the effectiveness of CNS in strengthening defective C-S-H structures in the x - direction where the tensile and compressive stresses are applied along the CNS chain direction. As shown in Fig. 11c, the CNS heals defective C-S-H structures by improving their tensile strength. For example, the tensile strength of the plain C-S-H is increased due to the inclusion of CNS by as much as 36.32% at Ca/Si = 1.1 (i.e., lowly-defective C-S-H) and 74.98% at Ca/Si = 2.1 (i.e., highly-defective C-S-H) (see Table S3). Under compression (see Fig.11d), the CNS seems to heal the defective C-S-H structures with Ca/Si ratios higher than 1.3 where the compressive strength of the C-S-H is increased by as much as 30.37% at Ca/Si = 2.1 (see Table S3).

The healing effect of CNS in the y - direction is shown in Fig. S9. A moderate increase in the tensile strength (between 10%~17%) is obtained for the C-S-H/CNS with Ca/Si ratios higher than 1.5. The increase in the compressive strength is between 20%-30% over the Ca/Si ratio range. In the z - direction, the increase in the tensile strength reaches up to 35% when the

Ca/Si ratio is 2.1, which is much higher than that in the y- direction. This is attributed to the ionic bonds established between the CNS functional groups and the calcium silicate sheets. Similar to the trend in tension, the C-S-H/CNS nanocomposite shows significant increase in the compressive strength, between 24.13% and 41.42% over the Ca/Si ratio range. The above findings indicate that overall, the CNS is more effective in healing highly-defective C-S-H, the main hydration phase of OPC than lowly-defective C-S-H. Table S3 summarizes the percentage of strength increase under tension and compression for all samples.

4. Conclusion

We have demonstrated the feasibility of using carrot-based cellulose nanosheets, sourced from inexpensive biomass, as a low-cost and environmentally friendly material for reinforcing highly deficient C-S-H, the main hydration product of cement. We performed MD simulations in conjunction with experimental characterization to gain fundamental understanding of the reinforcement effect of the CNS inserted into C-S-H with different Ca/Si ratios and uncover the interaction mechanisms at the atomic level between C-S-H and the CNS. Based on the combined MD simulations and experimental characterization, the following conclusions can be drawn:

(1). The CNSs show remarkable affinity to C-S-H due to the interfacial Ca-O coordination and H-bond interaction. The functional groups on the surface of the CNS were found to act like a root network confined by the surrounding bulk water molecules at the ITZ, thereby cross-linking the neighboring silicate calcium layers. This significantly improves the interfacial properties of the C-S-H/CNS hybrid structure. We also discovered that the water molecules between the C-S-H structures tend to migrate towards the intercalated CNSs. The water migration towards CNS transforms the layered C-S-H structure into a more amorphous state with increased interfacial Ca-O coordination number, thereby producing better structural stability and stronger interfacial properties. The retained water molecules in the CNS can further mitigate the water dynamics at the silicate nanochannel. As such, the water streaming

effect can be reduced and the cohesive force of the C-S-H gel can be improved.

(2). The incorporation of the CNSs can considerably improve the anisotropic constitutive behavior of C-S-H in terms of strength, stiffness and post-peak ductility at nano-scale. When the hybrid C-S-H/CNS structure is tensioned along the CNS chain direction, the tensile strength of the nanocomposite is increased by up to 75%, depending on the Ca/Si ratio. The reinforcing effect becomes more pronounced for disordered C-S-H structures. This is significant, because the poor performance of current cement-based materials is due to defective C-S-H gels resulting from high Ca/Si ratios. Thus, incorporating CNSs into cementitious materials would eliminate the need for costly and exhausting manufacturing processes to change the chemistry of the cement ingredients to achieve lower Ca/Si ratios for enhanced performance.

(3). The addition of the CNSs increases the compressive strength of C-S-H when the nanocomposite is loaded along the z - direction and perpendicular to the CNS surface. An increase up to 40% is achieved at the highest Ca/Si ratio. The addition of CNSs also enhances the compressive ductility of the C-S-H nanocomposite due to the strain-hardening effect resulting from the continuous confinement effect.

(4). Our experimental results clearly demonstrate that atomic-scale reinforcing mechanisms significantly improve the micro and macroscale properties of the cementitious composites containing CNSs sourced from inexpensive carrot waste streams. Compared to the plain cementitious composite, the nanocomposite with CNSs exhibited denser and better packed microstructure. The micromechanical properties of the nanocomposites are also improved when the CNSs are present. This improvement is more pronounced for the flexural strength due to the crack bridging effect.

The C-S-H reinforcement approach introduced here will aid efforts to design new generations of concrete materials with lower carbon footprint, by lowering the associated CO₂ emissions during cement production for the construction industry. When compared to current

cement reinforcing materials such as CNTs, graphene, GO and h-BN, the proposed CNS reinforcing material is inexpensive, renewable, carbon neutral, and has low environmental, health and safety risks. Furthermore, the CNSs are readily dispersible in water without the use of surface modification or surfactant and more importantly are highly compatible with C-S-H, the main hydration phase of cement. These features identify CNSs as a promising material for the production of sustainable and high-performance concretes. By increasing the performance of concrete, structural concrete elements with smaller sizes can be designed, thus reducing the volume of concrete, which in return reduces the energy and carbon intensity of the cement in the construction industry.

Data availability statement

The raw/processed data required to reproduce these findings cannot be shared at this time as the data also forms part of an ongoing study.

Acknowledgement

This research work is financially supported by the European Commission Horizon 2020 Marie Skłodowska-Curie Research Grant (B-SMART 799658). The authors would like to thank Cellucomp Ltd, Burntisland, UK for designing and manufacturing the CNSs. The authors are also grateful for the support from the China International Collaboration Fund (G20190017133).

Reference

- [1] Monteiro PJM, Miller SA, Horvath A. Towards sustainable concrete. *Nat Mater* 2017;16:698–9.
- [2] Norhasri MSM, Hamidah MS, Fadzil AM. Applications of using nano material in concrete: A review. *Constr Build Mater* 2017;133:91–7.
- [3] Senff L, Tobaldi DM, Lucas SS, Hotza D, Ferreira VM, Labrincha JA. Formulation of mortars with nano-SiO₂ and nano-TiO₂ for degradation of pollutants in buildings. *Compos Part B Eng* 2013;44:40–7.
- [4] Zhu Z, Xu W, Chen H, Tan Z. Evolution of microstructures of cement paste via continuous-based hydration model of non-spherical cement particles. *Compos Part B Eng* 2020;185:107795.
- [5] Xue G, Yilmaz E, Song W, Cao S. Mechanical, flexural and microstructural properties of cement-tailings matrix composites: effects of fiber type and dosage. *Compos Part B Eng* 2019;172:131–42.
- [6] Shahsavari R. Intercalated Hexagonal Boron Nitride/Silicates as Bilayer Multifunctional Ceramics. *ACS Appl Mater Interfaces* 2018;10:2203–9.
- [7] Yang H, Cui H, Tang W, Li Z, Han N, Xing F. A critical review on research progress of graphene/cement based composites. *Compos Part A Appl Sci Manuf* 2017;102:273–96.
- [8] Zhou C, Li F, Hu J, Ren M, Wei J, Yu Q. Enhanced mechanical properties of cement paste by hybrid graphene oxide/carbon nanotubes. *Constr Build Mater* 2017;134:336–45.
- [9] Lv SH, Deng LJ, Yang WQ, Zhou QF, Cui YY. Fabrication of polycarboxylate/graphene oxide nanosheet composites by copolymerization for reinforcing and toughening cement composites. *Cem Concr Compos* 2016;66:1–9.
- [10] Li G, Zhang LW. Microstructure and phase transformation of graphene-cement composites under high temperature. *Compos Part B Eng* 2019;166:86–94.
- [11] Qureshi TS, Panesar DK, Sidhureddy B, Chen A, Wood PC. Nano-cement composite with graphene oxide produced from epigenetic graphite deposit. *Compos Part B Eng* 2019;159:248–58.
- [12] Gao Y, Jing HW, Chen SJ, Du MR, Chen WQ, Duan WH. Influence of ultrasonication on the dispersion and enhancing effect of graphene oxide–carbon nanotube hybrid nanoreinforcement in cementitious composite. *Compos Part B Eng* 2019;164:45–53.
- [13] Kirgiz MS. Green cement composite concept reinforced by graphite nano-engineered particle suspension for infrastructure renewal material. *Compos Part B Eng* 2018;154:423–9.
- [14] Zhou Y, Hou D, Geng G, Feng P, Yu J, Jiang J. Insights into the interfacial strengthening mechanisms of calcium-silicate-hydrate/polymer nanocomposites. *Phys Chem Chem Phys* 2018;20:8247–66.
- [15] Zhou Y, Hou D, Manzano H, Orozco CA, Geng G, Monteiro PJM, et al. Interfacial Connection Mechanisms in Calcium-Silicate-Hydrates/Polymer Nanocomposites: A Molecular Dynamics Study. *ACS Appl Mater Interfaces* 2017;9:41014–25.
- [16] Shalchy F and NR. Nanostructural Characteristics and Interfacial Properties of Polymer Fibers in Cement Matrix. *ACS Appl Mater Interfaces* 2015;7:17278–86.
- [17] Hou D, Yu J, Wang P. Molecular dynamics modeling of the structure, dynamics,

- energetics and mechanical properties of cement-polymer nanocomposite. *Compos Part B Eng* 2019;162:433–44.
- [18] Zhang W, Zou X, Wei F, Wang H, Zhang G, Huang Y, et al. Grafting SiO₂ nanoparticles on polyvinyl alcohol fibers to enhance the interfacial bonding strength with cement. *Compos Part B Eng* 2019;162:500–7.
 - [19] Yao X, Shamsaei E, Chen S, Zhang QH, de Souza FB, Sagoe-Crentsil K, et al. Graphene oxide-coated Poly (vinyl alcohol) fibers for enhanced fiber-reinforced cementitious composites. *Compos Part B Eng* 2019;174:107010.
 - [20] Zhou Y, Orozco CA, Duque-Redondo E, Manzano H, Geng G, Feng P, et al. Modification of poly(ethylene glycol) on the microstructure and mechanical properties of calcium silicate hydrates. *Cem Concr Res* 2019;115:20–30.
 - [21] Kumar A, Walder BJ, Kunhi Mohamed A, Hofstetter A, Srinivasan B, Rossini AJ, et al. The Atomic-Level Structure of Cementitious Calcium Silicate Hydrate – Supporting Information Table of Contents. *J Phys Chem C* 2017;121:17188–96.
 - [22] Xu L, Deng F, Chi Y. Nano-mechanical behavior of the interfacial transition zone between steel-polypropylene fiber and cement paste. *Constr Build Mater* 2017;145:619–38.
 - [23] Allen AJ, Thomas JJ, Jennings HM. Composition and density of nanoscale calcium-silicate-hydrate in cement. *Nat Mater* 2007;6:311–6.
 - [24] Chen B, Qiao G, Hou D, Wang M, Li Z. Cement-based material modified by in-situ polymerization: From experiments to molecular dynamics investigation. *Compos Part B Eng* 2020:108036.
 - [25] Hou D, Xu J, Zhang Y, Sun G. Insights into the molecular structure and reinforcement mechanism of the hydrogel-cement nanocomposite: An experimental and molecular dynamics study. *Compos Part B Eng* 2019;177:107421.
 - [26] Eftekhari M, Mohammadi S, Khanmohammadi M. A hierarchical nano to macro multiscale analysis of monotonic behavior of concrete columns made of CNT-reinforced cement composite. *Constr Build Mater* 2018;175:134–43.
 - [27] Ioannidou K, Krakowiak KJ, Bauchy M, Hoover CG, Masoero E, Yip S, et al. Mesoscale texture of cement hydrates. *Proc Natl Acad Sci* 2016;113:2029–34.
 - [28] Jennings HM, Bullard JW. From electrons to infrastructure: Engineering concrete from the bottom up. *Cem Concr Res* 2011;41:727–35.
 - [29] Ye J, Chu C, Cai H, Hou X, Shi B, Tian S, et al. A multi-scale model for studying failure mechanisms of composite wind turbine blades. *Compos Struct* 2019;212:220–9.
 - [30] Ye J, Chu C, Cai H, Wang Y, Qiao X, Zhai Z, et al. A multi-scale modeling scheme for damage analysis of composite structures based on the High-Fidelity Generalized Method of Cells. *Compos Struct* 2018;206:42–53.
 - [31] Tatar J, Taylor CR, Hamilton HR. A multiscale micromechanical model of adhesive interphase between cement paste and epoxy supported by nanomechanical evidence. *Compos Part B Eng* 2019;172:679–89.
 - [32] Birenboim M, Nadiv R, Alatawna A, Buzaglo M, Schahar G, Lee J, et al. Reinforcement and workability aspects of graphene-oxide-reinforced cement nanocomposites. *Compos Part B Eng* 2019;161:68–76.
 - [33] Kunhi Mohamed A, Parker SC, Bowen P, Galmarini S. An atomistic building block description of C-S-H - Towards a realistic C-S-H model. *Cem Concr Res* 2018;107:221–35.

- [34] Qomi MJA, Krakowiak KJ, Bauchy M, Stewart KL, Shahsavari R, Jagannathan D, et al. Combinatorial molecular optimization of cement hydrates. *Nat Commun* 2014;5:4960.
- [35] Pellenq RJ-M, Kushima A, Shahsavari R, Van Vliet KJ, Buehler MJ, Yip S, et al. A realistic molecular model of cement hydrates. *Proc Natl Acad Sci* 2009;106:16102–7.
- [36] Almeida APC, Canejo JP, Fernandes SN, Echeverria C, Almeida PL, Godinho MH. Cellulose-Based Biomimetics and Their Applications. *Adv Mater* 2018;30:1–31.
- [37] Shchipunov Y, Postnova I. Cellulose Mineralization as a Route for Novel Functional Materials. *Adv Funct Mater* 2018;28:1–28.
- [38] Moon RJ, Martini A, Nairn J, Simonsen J, Youngblood J. Cellulose nanomaterials review: structure, properties and nanocomposites. *Chem Soc Rev* 2011;40:3941–94.
- [39] Mazeau K, Heux L. Molecular dynamics simulations of bulk native crystalline and amorphous structures of cellulose. *J Phys Chem B* 2003;107:2394–403.
- [40] Portugal I, Dias VM, Duarte RF, Evtuguin D V. Hydration of cellulosesilica hybrids assessed by sorption isotherms. *J Phys Chem B* 2010;114:4047–55.
- [41] Alshaghel A, Parveen S, Rana S, Fangueiro R. Effect of multiscale reinforcement on the mechanical properties and microstructure of microcrystalline cellulose-carbon nanotube reinforced cementitious composites. *Compos Part B Eng* 2018;149:122–34.
- [42] Hasan H, Huang B, Saafi M, Sun J, Chi Y, Whale E, et al. Novel engineered high performance sugar beetroot 2D nanoplatelet-cementitious composites. *Constr Build Mater* 2019;202:546–62.
- [43] Chen P, Ogawa Y, Nishiyama Y, Ismail AE, Mazeau K. Linear, non-linear and plastic bending deformation of cellulose nanocrystals. *Phys Chem Chem Phys* 2016;18:19880–7.
- [44] Rahman R, Foster JT, Haque A. Molecular dynamics simulation and characterization of graphene–cellulose nanocomposites. *J Phys Chem A* 2013;117:5344–53.
- [45] Bergensträhle M, Wohler J, Himmel ME, Brady JW. Simulation studies of the insolubility of cellulose. *Carbohydr Res* 2010;345:2060–6.
- [46] Hou D, Yu J, Jin Z, Hanif A. Molecular dynamics study on calcium silicate hydrate subjected to tension loading and water attack: structural evolution, dynamics degradation and reactivity mechanism. *Phys Chem Chem Phys* 2018;20:11130–44.
- [47] Morshedifard A, Masoumi S, Qomi MJA. Nanoscale origins of creep in calcium silicate hydrates. *Nat Commun* 2018;9:1–10.
- [48] Richardson IG. The calcium silicate hydrates. *Cem Concr Res* 2008;38:137–58.
- [49] Fan D, Yang S. Mechanical properties of CSH globules and interfaces by molecular dynamics simulation. *Constr Build Mater* 2018;176:573–82.
- [50] Hepworth D, Whale E. Cellulose platelet compositions, methods of preparing cellulose platelet compositions and products comprising same. US 9,834,664 B2, 2017.
- [51] ASTM C109 A. Standard test method for compressive strength of hydraulic cement mortars (Using 2-in. or [50-mm] cube specimens). *Am Soc Test Mater* 2002.
- [52] ASTM C. Standard test method for flexural strength of concrete (using simple beam with third-point loading). *Am. Soc. Test. Mater.*, vol. 100, 2010, p. 12959–9428.
- [53] Plimpton S. Fast parallel algorithms for short-range molecular dynamics. *J Comput Phys* 1995;117:1–19.
- [54] Stukowski A. Visualization and analysis of atomistic simulation data with OVITO—the Open Visualization Tool. *Model Simul Mater Sci Eng* 2009;18:15012.
- [55] Nishiyama Y, Sugiyama J, Chanzy H, Langan P. Crystal structure and hydrogen

- bonding system in cellulose Ia from synchrotron X-ray and neutron fiber diffraction. *J Am Chem Soc* 2003;125:14300–6.
- [56] Nishiyama Y, Langan P, Chanzy H. Crystal structure and hydrogen-bonding system in cellulose Ib from synchrotron X-ray and neutron fiber diffraction. *J Am Chem Soc* 2002;124:9074–82.
- [57] Bahafid S, Ghabezloo S, Duc M, Faure P, Sulem J. Effect of the hydration temperature on the microstructure of Class G cement: CSH composition and density. *Cem Concr Res* 2017;95:270–81.
- [58] Hamid SA. The crystal structure of the 11Å natural tobermorite. *Zeitschrift Fur Krist* 1981;8:1–10.
- [59] Cygan RT, Liang J-J, Kalinichev AG. Molecular models of hydroxide, oxyhydroxide, and clay phases and the development of a general force field. *J Phys Chem B* 2004;108:1255–66.
- [60] Dauber-Osguthorpe P, Roberts VA, Osguthorpe DJ, Wolff J, Genest M, Hagler AT. Structure and energetics of ligand binding to proteins: Escherichia coli dihydrofolate reductase- trimethoprim, a drug- receptor system. *Proteins Struct Funct Bioinforma* 1988;4:31–47.
- [61] Berendsen HJC, Grigera JR, Straatsma TP. The missing term in effective pair potentials. *J Phys Chem* 1987;91:6269–71.
- [62] Hou D, Ma H, Zhu Y, Li Z. Calcium silicate hydrate from dry to saturated state: structure, dynamics and mechanical properties. *Acta Mater* 2014;67:81–94.
- [63] Mead RN, Mountjoy G. a molecular dynamics study of the atomic structure of (CaO) x (SiO₂) 1-x Glasses. *J Phys Chem B* 2006;110:14273–8.
- [64] Manzano H, Moeini S, Marinelli F, Van Duin ACT, Ulm F-J, Pellenq RJ-M. Confined water dissociation in microporous defective silicates: mechanism, dipole distribution, and impact on substrate properties. *J Am Chem Soc* 2012;134:2208–15.
- [65] Bonnaud PA, Ji Q, Coasne B, Pellenq R-M, Van Vliet KJ. Thermodynamics of water confined in porous calcium-silicate-hydrates. *Langmuir* 2012;28:11422–32.

Figures

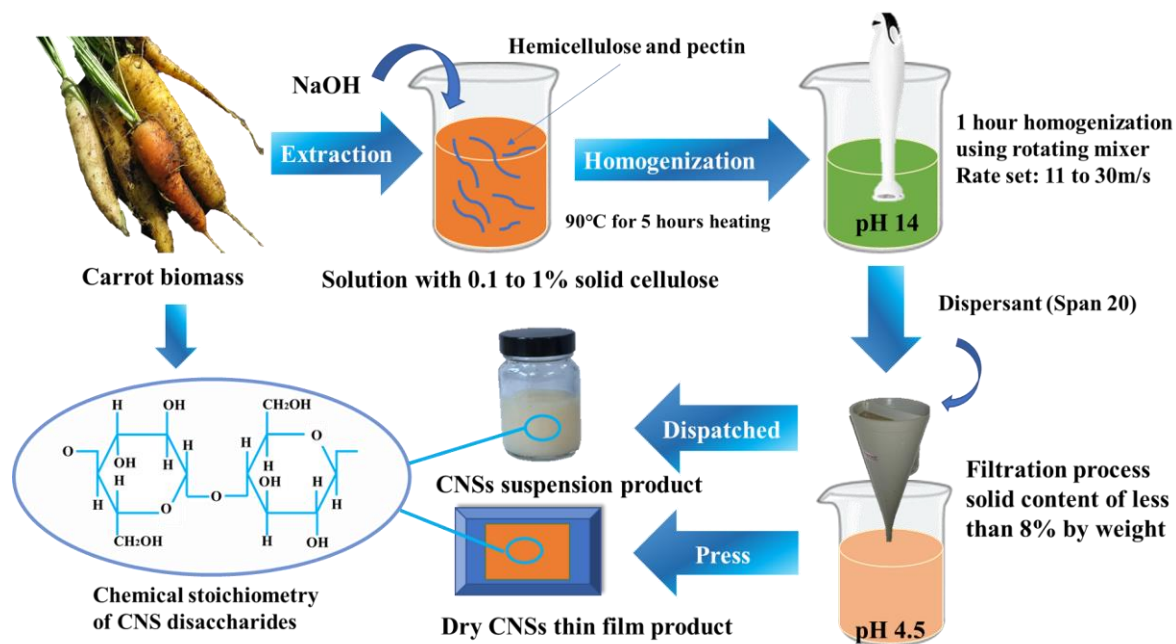


Fig.1 Schematic diagram of CNSs fabrication process

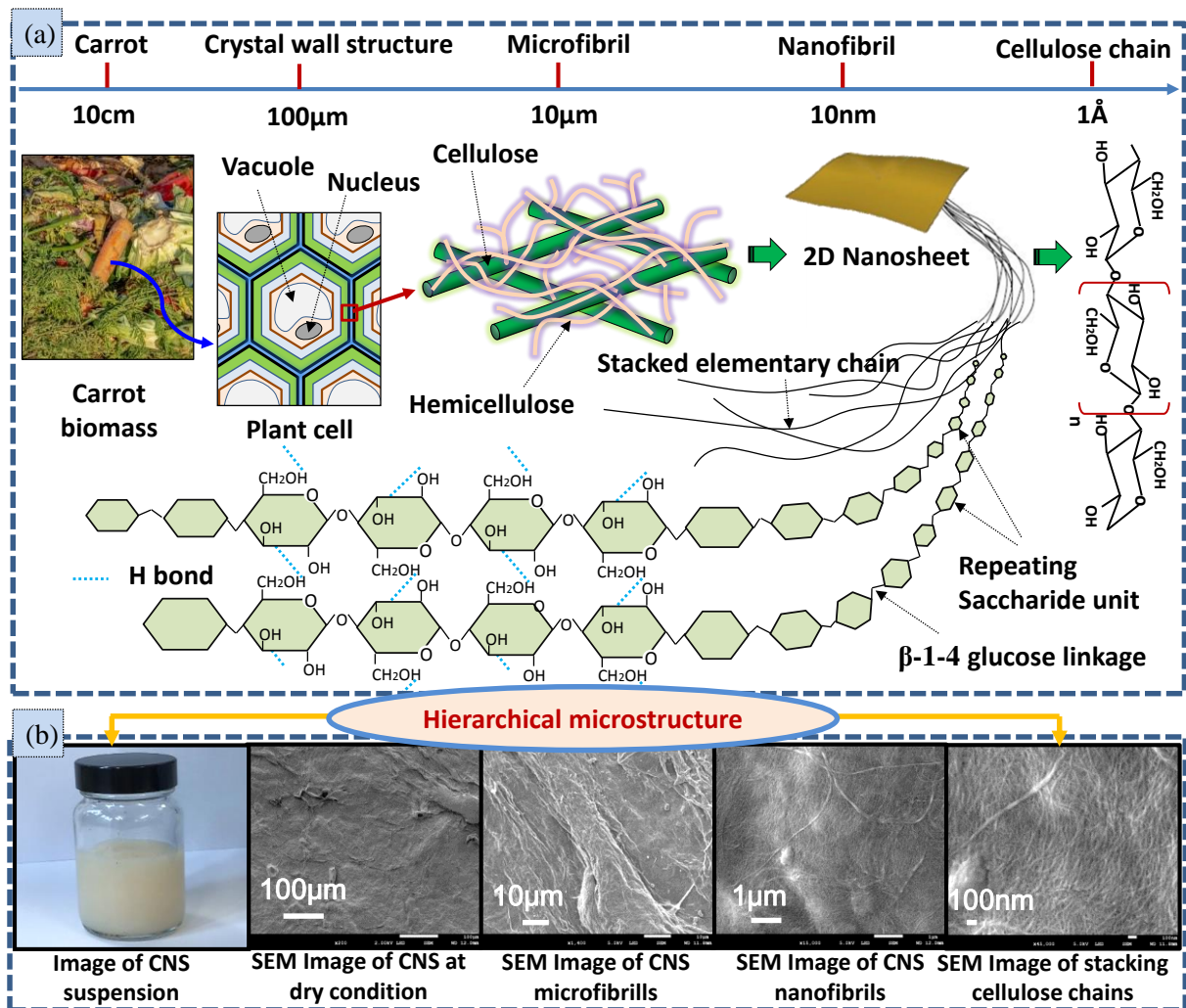


Fig. 2. The crystallographic of the 2D CNS sheets from waste stream: (a) Hierarchical microstructure of the CNS. (b) Images of the CNS from a CNS suspension to nanofibrils forming CNS at different length scales.

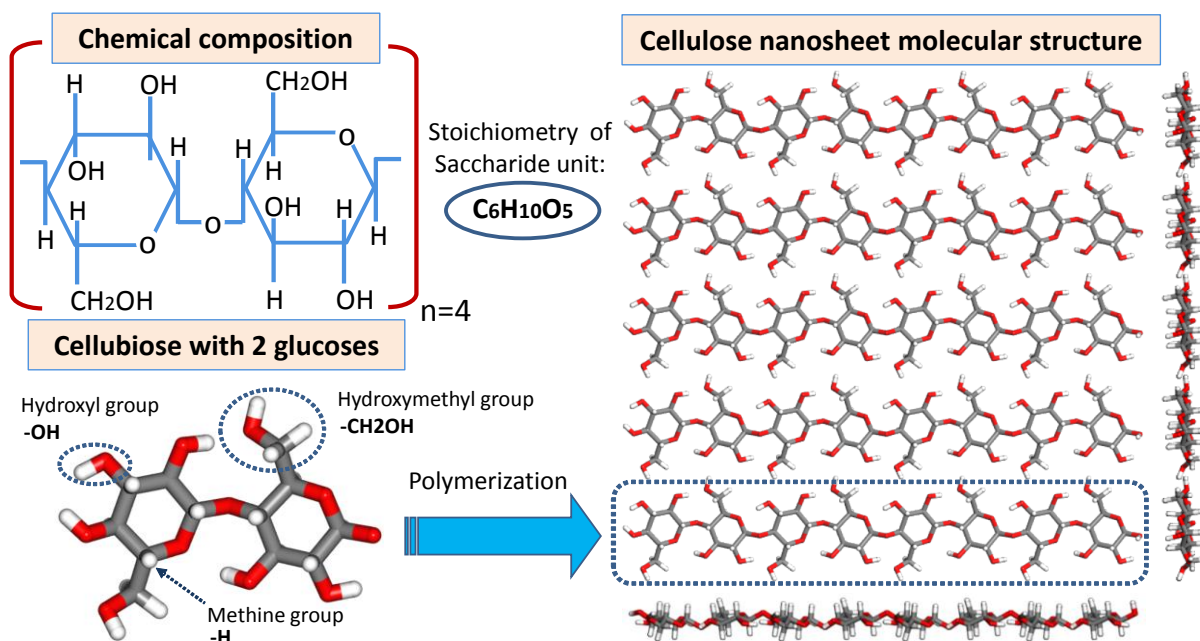


Fig. 3. Molecular structure of the CNS and the corresponding chemical stoichiometry of one saccharide unit. The black, red and white sticks in the molecular model of CNS represent carbon, oxygen and hydrogen atoms respectively.

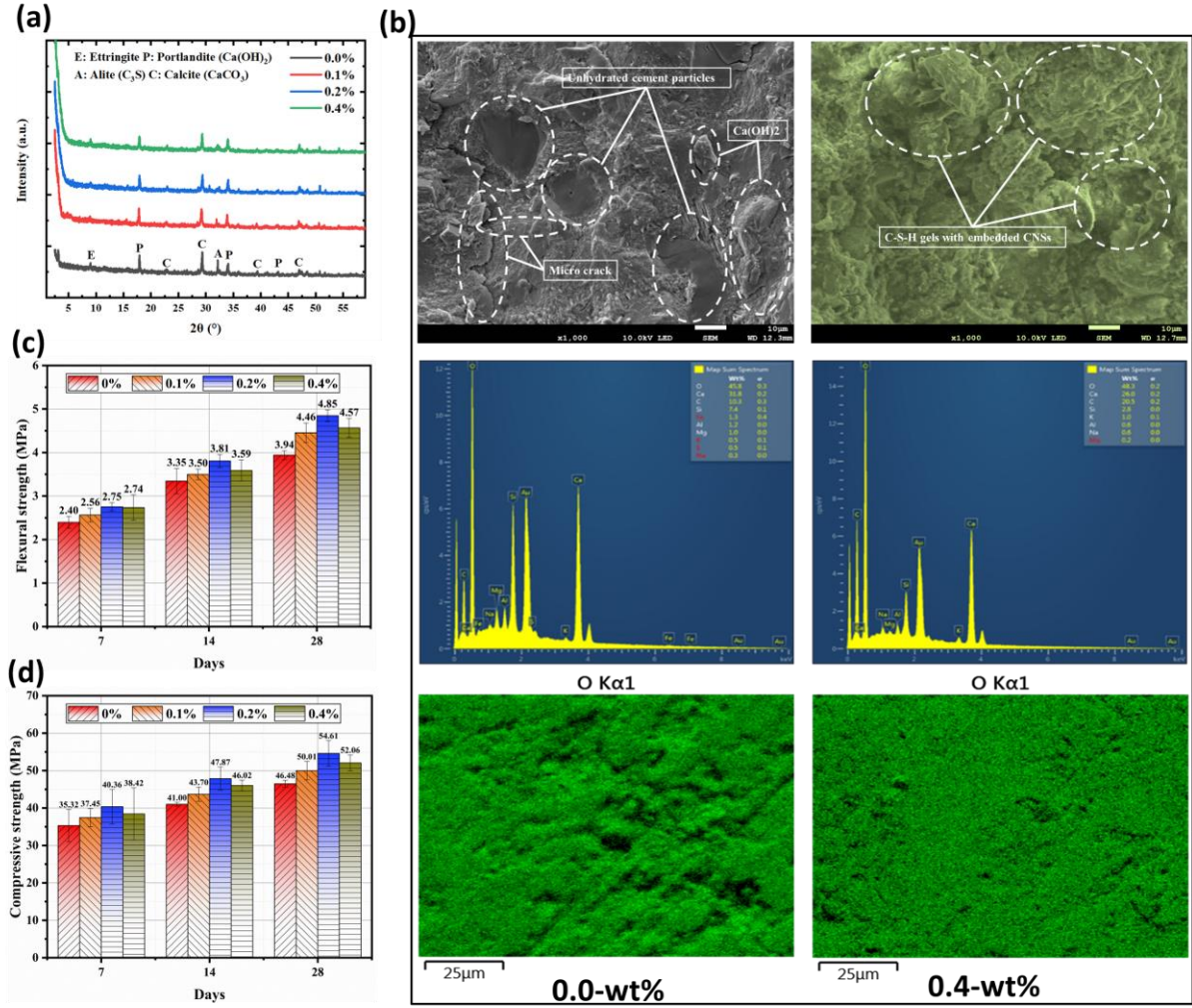


Fig. 4. Microstructure characterization and mechanical properties of CNS cementitious composites with different CNS mass fractions. (a) XRD patterns. (b) SEM-EDX images. (c) Flexural strengths. (d) Compressive strengths.

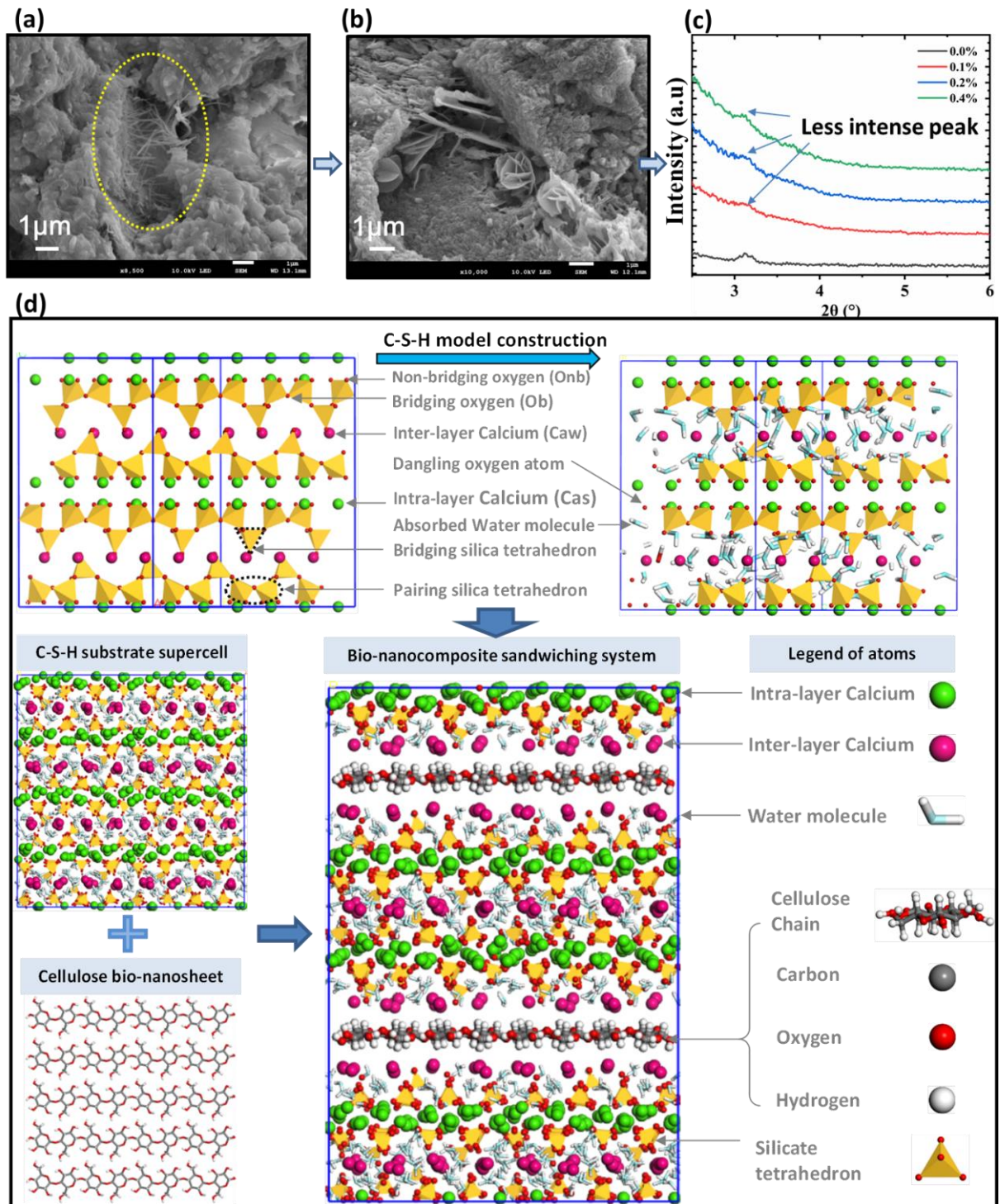


Fig. 5. Microstructural configurations of the nanocomposite. (a-b) SEM images of intercalated cellulose chain and CNS. (c) XRD patterns showing the concentration of CNS with a broader and less peak at $\approx 3^\circ 2\theta$. (d) Constructed molecule model for nanocomposite bilayer system.

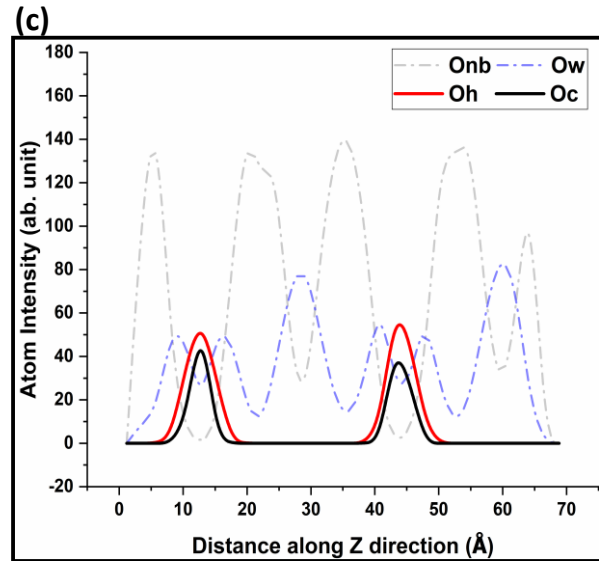
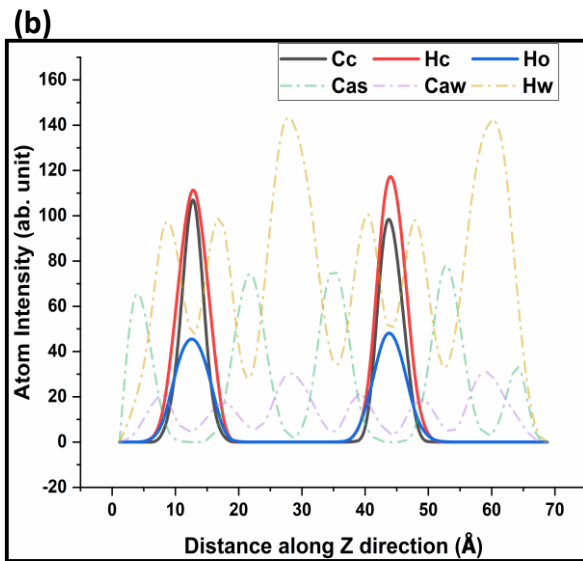
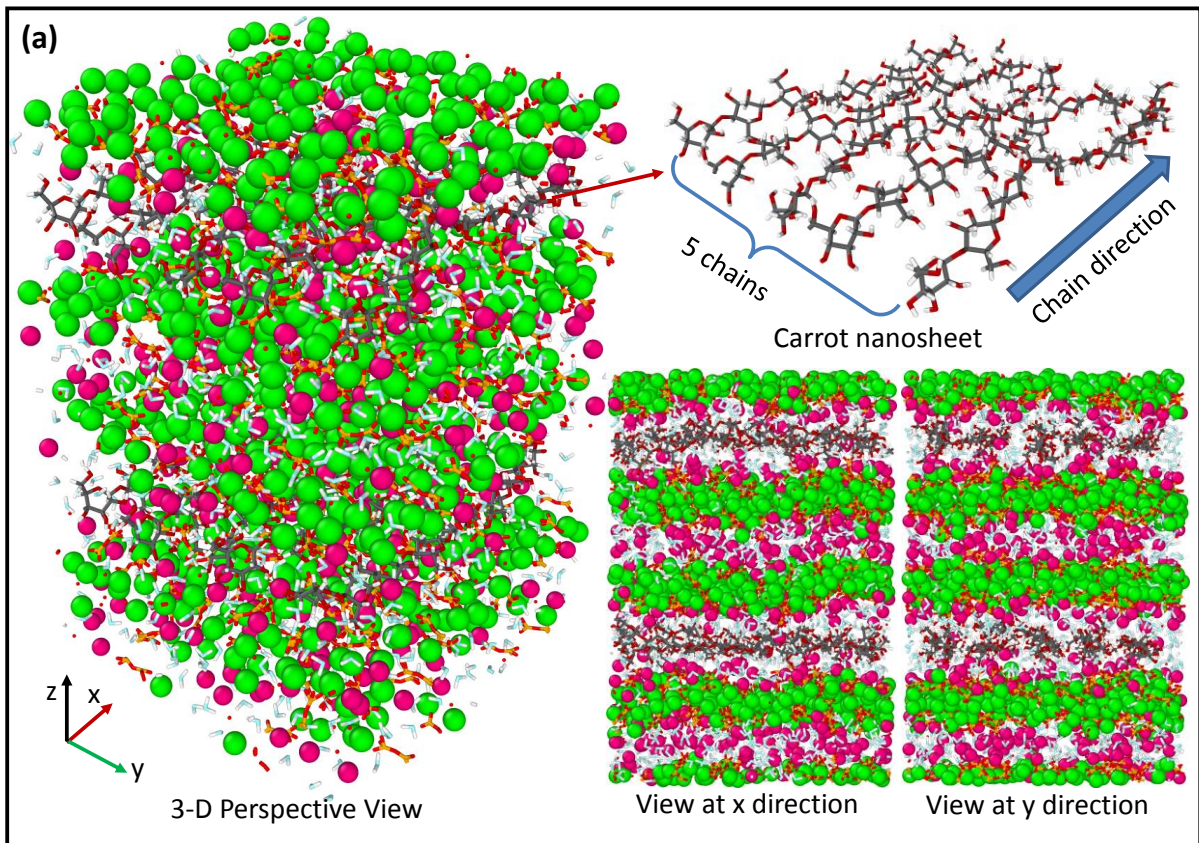


Fig. 6. Relaxed molecular structural configuration. (a) Evolved molecular model after NPT equilibrium. (b) Atom intensity distributions of different atoms at the ITZ region. (c) Atom density distributions of oxygen species from both CNS and C-S-H gel. In the atomistic configurations, the green and purple spheres represent the inter- and intra-layer calcium atoms, red balls denote the oxygen atom, black balls are the carbon atom, white balls show the hydrogen atoms, light blue-white ball stick model represents the water molecule, yellow-red bond denotes the silicate chain (Si-O), black-red-white stick model represents the CNS chain, yellow tetrahedral shaped models are the silicate tetrahedra.

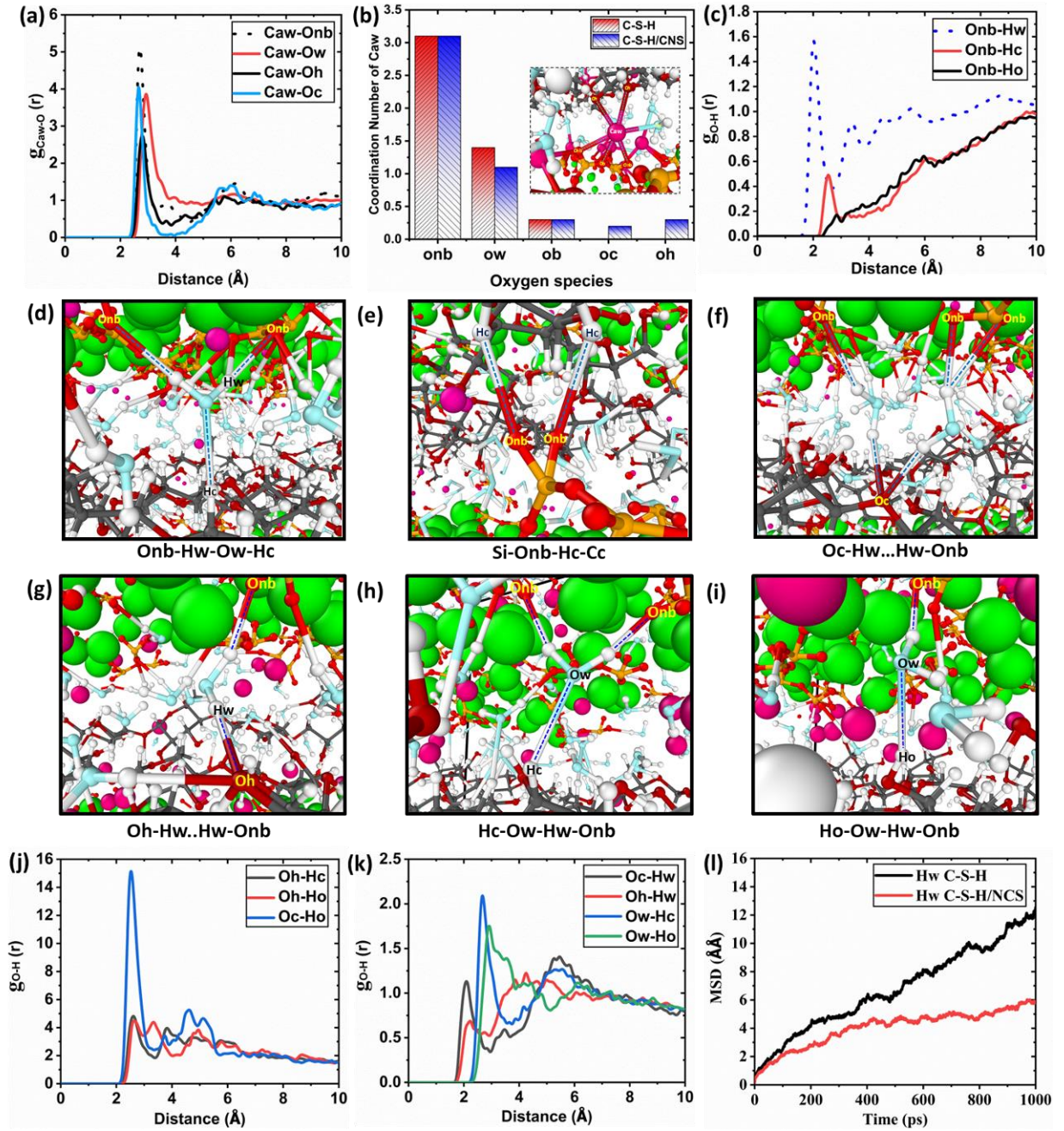


Fig. 7. Local structural characteristics of CNS at the ITZ. (a) Partial RDF between interlayer calcium from C-S-H versus different oxygen species. (b) Coordination number of different O species for pure C-S-H and nanocomposite. (c) Partial RDF between Onb versus different hydrogen Species. (d-i) Representative H-bond network in the ITZ region. (j) Partial RDF distribution between oxygen species and hydrogen species within CNS. (k) Partial RDF between oxygen and hydrogen atoms from CNS and water molecule. (l) Comparison of MSD evolution of interlayer water hydrogen atoms for the molecular systems with and without CNS. In the atomic configuration, the green, purple, yellow, red, light blue, black, dark red, white spheres represent the intra-layer calcium, inter-layer calcium, silicon, silicate oxygen, water oxygen, carbon, CNS oxygen, hydrogen atoms respectively.

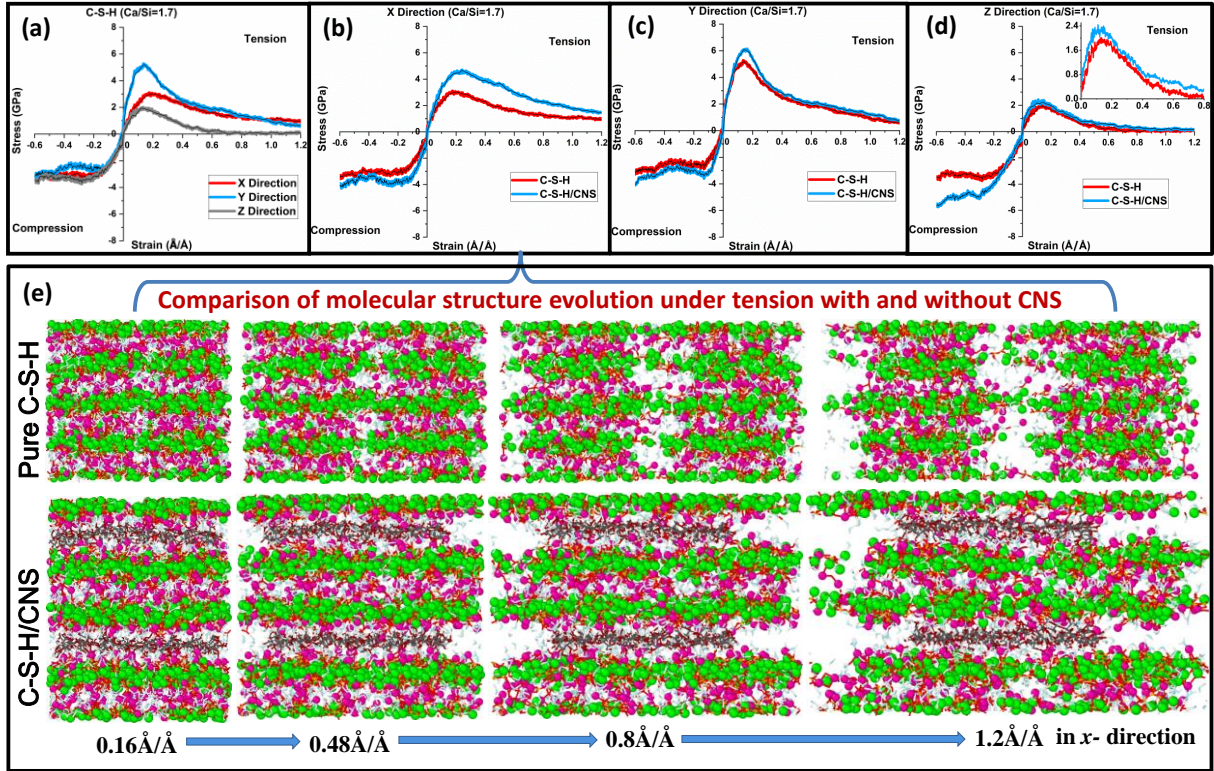


Fig. 8. Anisotropic nanomechanical properties. (a-d) Comparison of the computed stress-strain curves between the C-S-H and nanocomposite along x -, y - and z - direction under uniaxial deformation with $\text{Ca/Si}=1.7$. (e) Comparison of typical molecular structural evolutions under tension in x - direction. For the colored molecular configuration, the green and purple spheres represents the inter- and intra-layer calcium atoms, red balls denote the oxygen atom, light blue-white ball stick model represents the water molecule, yellow-red bond denotes the silicate chain(Si-O), black-red-white stick model represents the CNS chain.

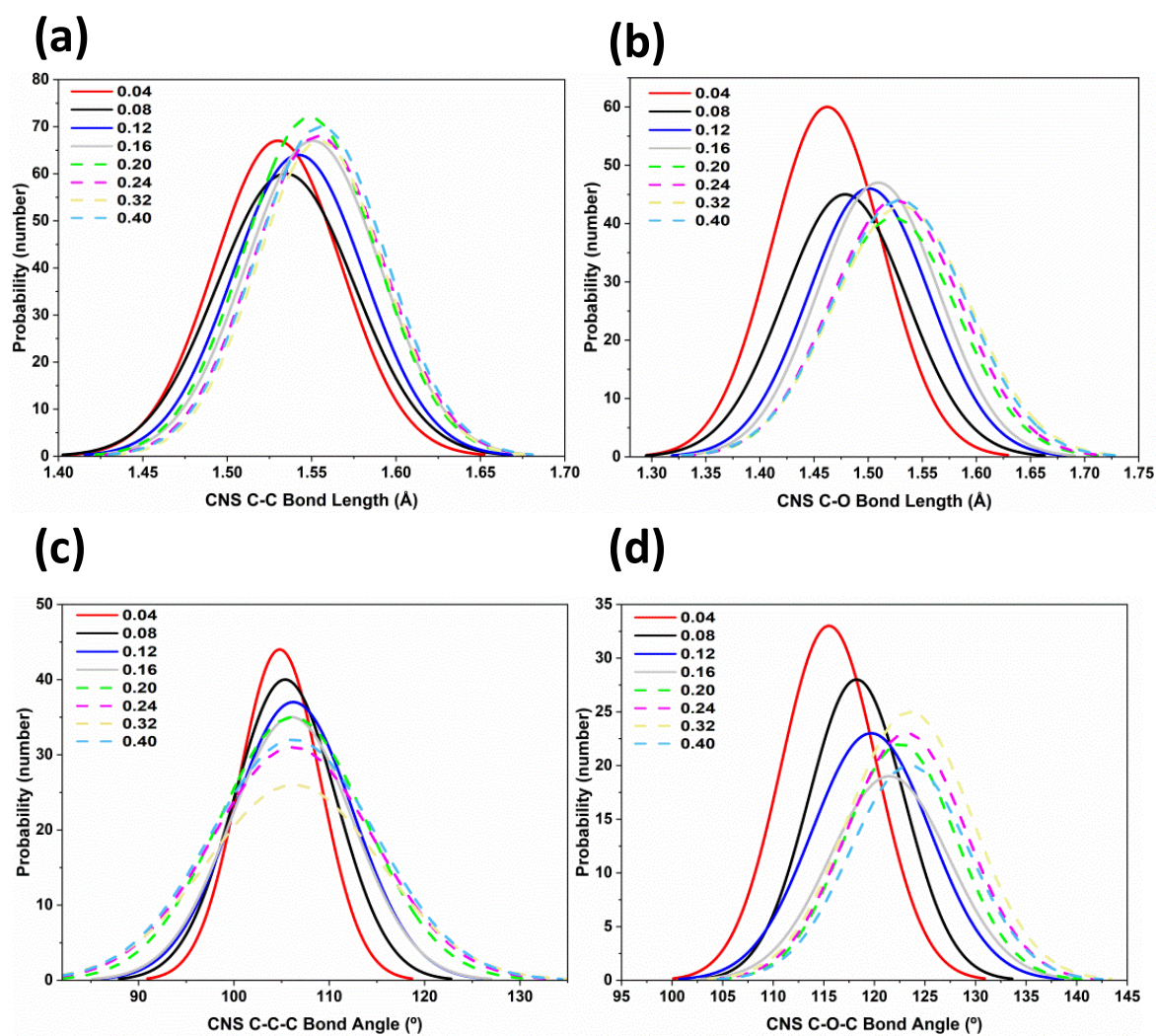


Fig. 9. BLE and BAD distributions of CNS chain during loading (a)C-C bond length distribution. (b) C-O bond length distribution. (c) C-C-C bond angle distribution. (d) C-O-C bond angle distribution.

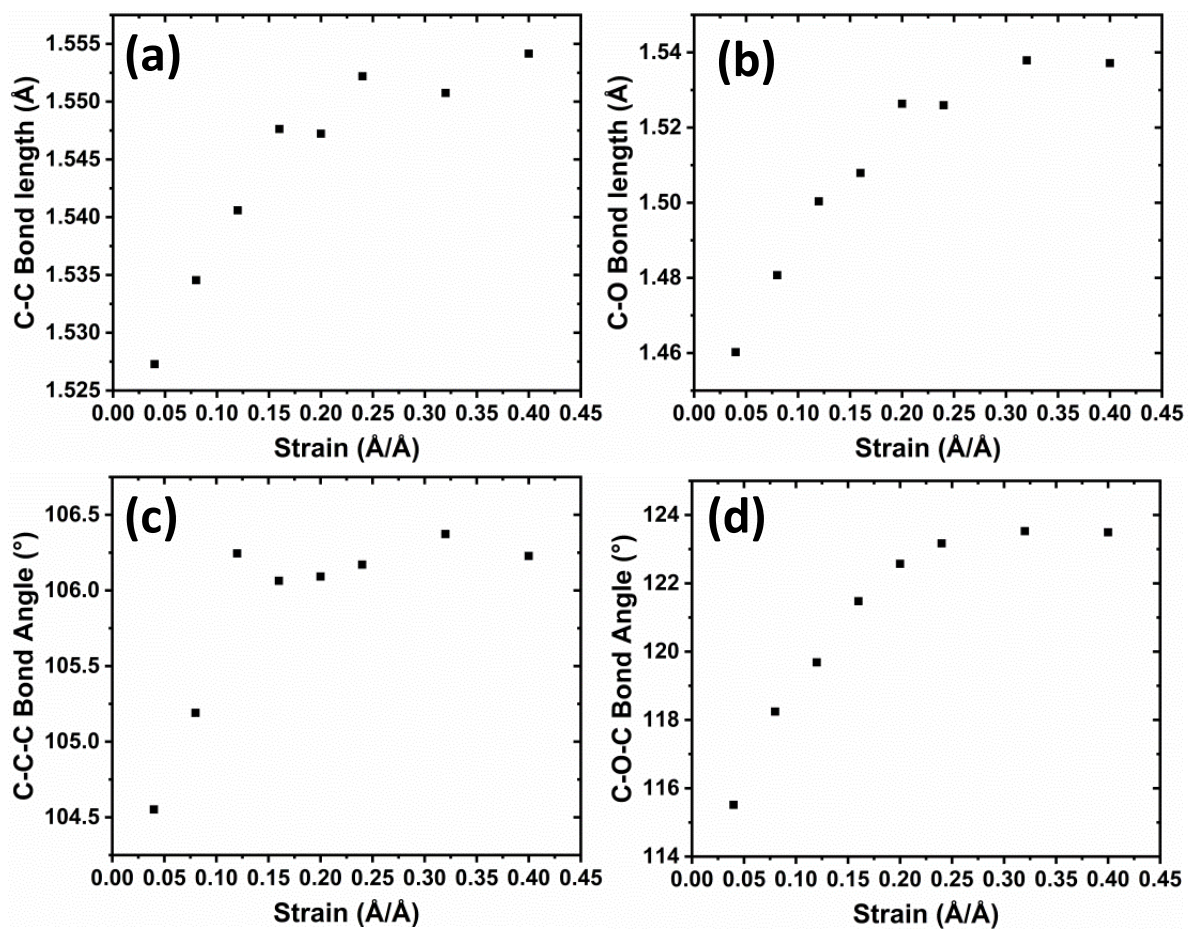


Fig. 10. Evolution of mean bond length/angle values with increasing tensile strain (a) C-C bond length evolution. (b) C-O bond length evolution. (c) C-C-C bond angle evolution. (d) C-O-C bond angle evolution.

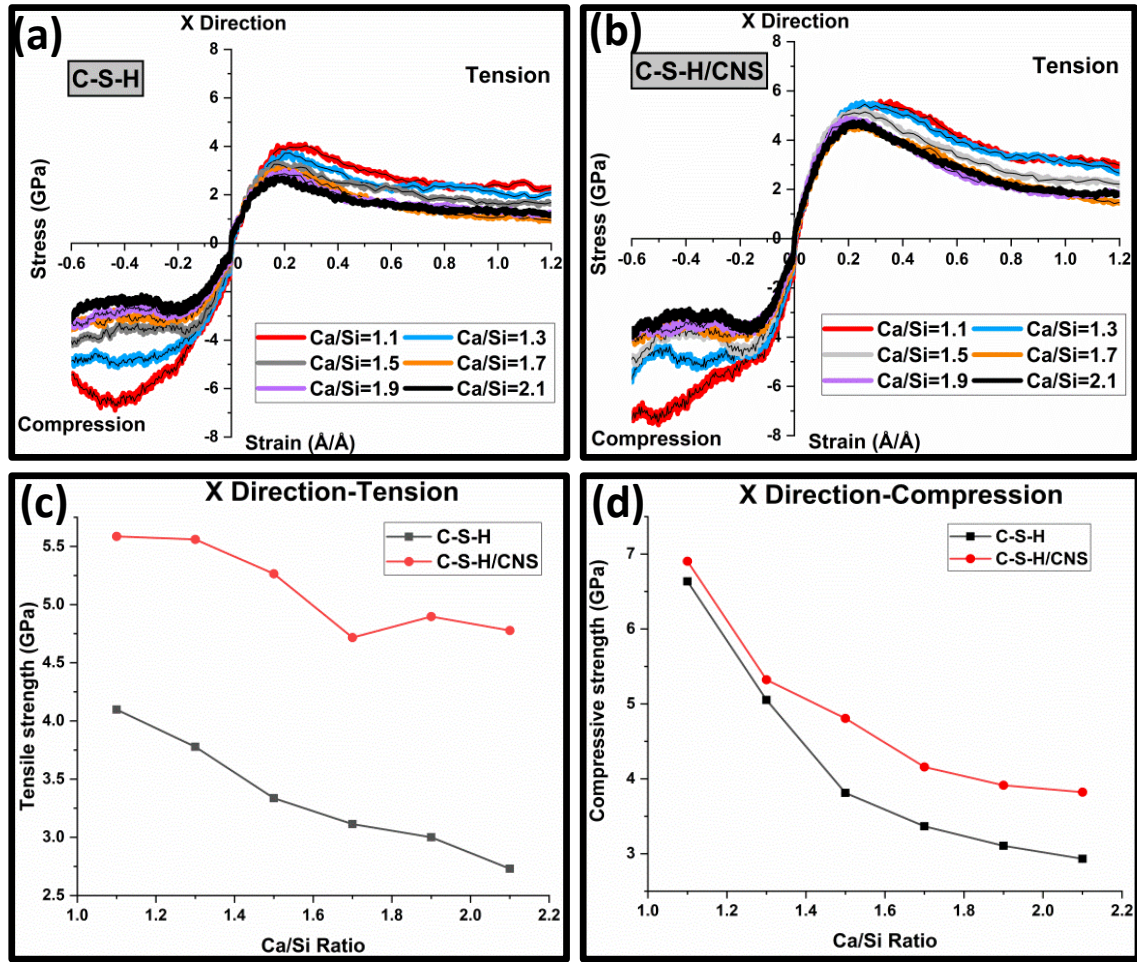
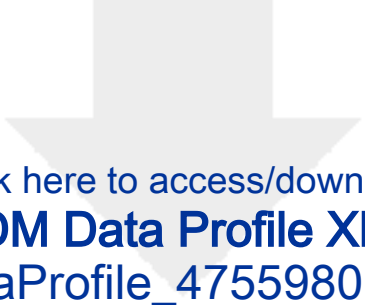


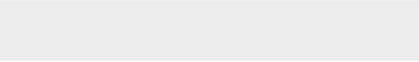
Fig. 11. Variation of nanomechanical behavior at different Ca/Si ratios. (a-b) Stress-strain responses of the C-S-H and C-S-H/CNS nanocomposite in the x -direction. (c-d) The effectiveness of CNS in strengthening defective C-S-H structures in the x -direction for tension and compression

Supporting Information

The following files are available free of charge. Supporting information (Word).



Click here to access/download
RDM Data Profile XML
DataProfile_4755980.xml



Declaration of interests

☒ The authors declare that they have no known competing financial interests or personal relationships that could have appeared to influence the work reported in this paper.

☐The authors declare the following financial interests/personal relationships which may be considered as potential competing interests:

Mohamed Saafi : Conceptualization, Writing - Review & Editing, Supervision, Funding acquisition. **Yin Chi**: Methodology, Software, Formal analysis, Writing - Original Draft, **Bo Huang**: Investigation, Resources, Data Curation. **Jianqiao Ye**: Validation, Writing - Review & Editing and Project administration. **Colin Lambert**: Writing - Review & Editing

Carrot-based covalently bonded saccharides as a new 2D material for healing defective calcium-silicate-hydrate in cement: Integrating atomistic computational simulation with experimental studies

Yin Chi,^{a,b*} Bo Huang,^b Mohamed Saafi,^{b*} Jianqiao Ye,^b Colin Lambert^c

^a School of Civil Engineering, Wuhan University, Wuhan 430072, China

^b Department of Engineering, Lancaster University, Lancashire, LA1 4YW, UK

^c Department of Physics, Lancaster University, Lancashire, LA1 4YB, UK

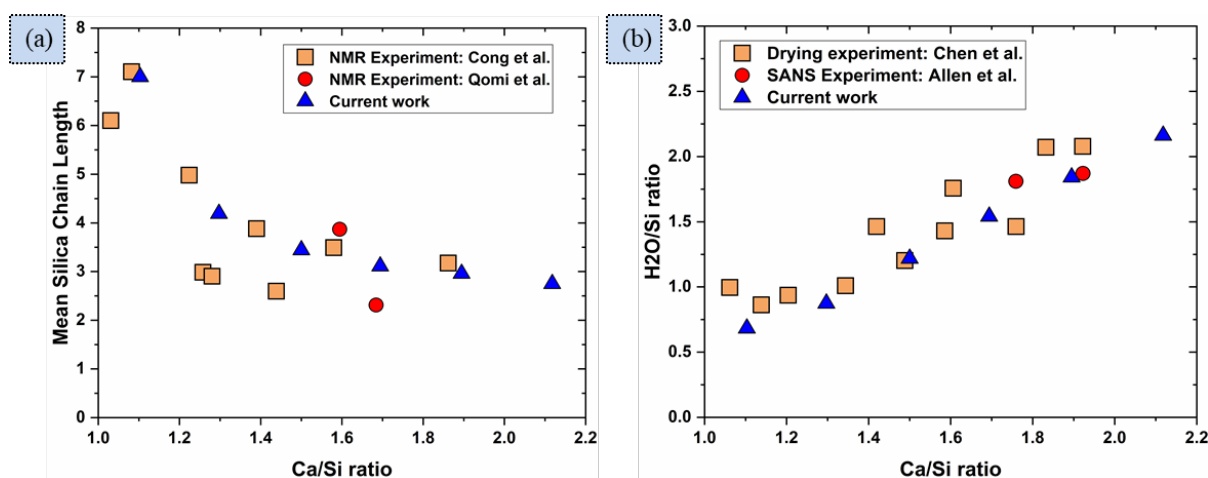


Fig. S1. Effect of Ca/Si ratio on the molecular structure of C-S-H and the comparisons between the constructed model and experiments: a) MCL; b) H₂O/Si ratio

It is known that the chemical composition of C-S-H differs significantly not only among different samples but also within one given paste. The calcium to silicon (Ca/Si) ratio is found to vary between 1.2 and 2.1 with an average of ≈ 1.7 as evidenced from transmission electron microscopy (TEM) and electron microscope analysis EMPA[1]. The variation in Ca/Si ratio during hydration probably occurs due to the variation in dissolved calcium concentration in the aqueous solution[2]. Therefore, in this paper, 6 C-S-H substrate samples with Ca/Si ratios of 1.1, 1.3, 1.5, 1.7, 1.9 and 2.1 are considered, which covers the typical range gleaned from experimental observations of C-S-H products. The tobermorite 11 Å model proposed by Hamid[3] is taken as an atomic structural benchmark of the C-S-H substrate, which has a layered crystalline structure composed of infinite “dreierketten” silicate chains with a chemical stoichiometry of $(\text{Ca}_5[\text{Si}_6\text{O}_{16}(\text{OH})_2] \cdot 2\text{H}_2\text{O})$. First, the water molecules and hydroxyl groups are removed from the initial Hamid model to attain an anhydrate monoclinic 11 Å tobermorite structure, which is then transformed into an orthorhombic cell that has crystal lattice parameters of $a=22.32 \text{ Å}$, $b=22.17 \text{ Å}$, $c=22.77 \text{ Å}$ and $\alpha=\beta=\gamma=90^\circ$.

deg according to Merlino, et al.[4] The orthorhombic cell contains infinite silica chains and calcium atoms categorized in two distinct environments as intra-layer calcium and inter-layer calcium between adjacent calcium-silicate sheets (referred as C_{as} and C_{aw} hereafter). To construct a realistic molecular model of C-S-H that is similar to those modern hydrated cement, a suitable number of charge-neutral SiO_2 groups at random locations are removed from the silicate chains to achieve different Ca/Si ratios[5]. The original infinitely long silica chains are then substituted by a combination of monomers, dimers, pentamers and octamer of silicate tetrahedra. The constructed defective structures with missing bridging and pairing silicate tetrahedra can both decrease the chain length and increase the Ca/Si ratio, which is shown to be in close agreements with the Q_n species distribution probed from ^{29}Si nuclear magnetic resonance (NMR) tests[6,7]. The comparison of the mean silica chain length (MCL) between the constructed models and the test results are shown in Fig. S1a. Thereafter, the water sorption simulation is performed for the above orthorhombic C-S-H crystal structures based on the Metropolis Monte Carlo method with Grand canonical ensemble[8]. During the sorption simulation, a fixed ambient pressure of 1 atmosphere and the temperature of $T=300$ Kelvin are set. This water sorption procedure provides five types of operations for a grand canonical ensemble, i.e., conformer, rotation, translation, creation and deletion of the water sorbate are attempted. Equilibrium runs of 3 million steps are specified to reach system equilibrium, followed by production runs of 1 million steps to reach a saturated state of the C-S-H model. It should be noted that, the anhydrate C-S-H with different Ca/Si ratio have different water sorption capacities[9]. Taking the C-S-H model with a Ca/Si ratio of 1.7 as an example, the constructed model at a saturated state gives a final chemical stoichiometry of $(CaO)_{1.69}(SiO_2)(H_2O)_{1.54}$ and a density of approximate $2.44g\ cm^{-3}$, which is in line with the observations from small angle neutral scattering (SANS) experiments[7]. The comparison of the computed H_2O/Si ratios with the reported SANS and drying experiments[10] for C-S-H having various Ca/Si ratios are shown in Fig. S1b, and the critical atomic textural information of the above constructed C-S-H models is summarized in Table S1. Thereafter, the C-S-H crystal containing saturated water molecules is periodically replicated 2 times along the x -, y - and z - directions to create a super cell, of which the dimensions were $a=44.64\ \text{\AA}$, $b=44.34\ \text{\AA}$, $c=45.54\ \text{\AA}$, $\alpha=\beta=\gamma=90\ \text{deg}$, containing $4\times6\times2$ crystallographic unit cells and are close to an actual C-S-H gel nano particle size($\approx 5nm$). This super cell is used as the benchmark for constructing the nano-texture of the composite system (See Fig. S2).

Table S1. Summary of benchmarking C-S-H molecular model for different Ca/Si ratio

No.	Ca/Si ratio	Number of polymerization				Q _n species ^{a)} No.			MCL	H ₂ O/Si ratio
		monomer	dimer	pentamer	octamer	Q ₀	Q ₁	Q ₂		
wh11	1.103	0	2	2	14	0	36	90	7.000	0.6825
wh13	1.297	2	10	13	3	2	52	57	4.192	0.8739
wh15	1.500	3	14	13	0	3	54	39	3.444	1.2188
wh17	1.694	1	17	10	0	1	54	30	3.111	1.5412
wh19	1.895	2	17	8	0	2	50	24	2.960	1.8421
wh21	2.118	2	18	6	0	2	48	18	2.750	2.1618

^{a)} Q_n species refers to silicon atoms that are covalently bonded to other *n* silicon atoms via bridging oxygen with $0 < n < 4$

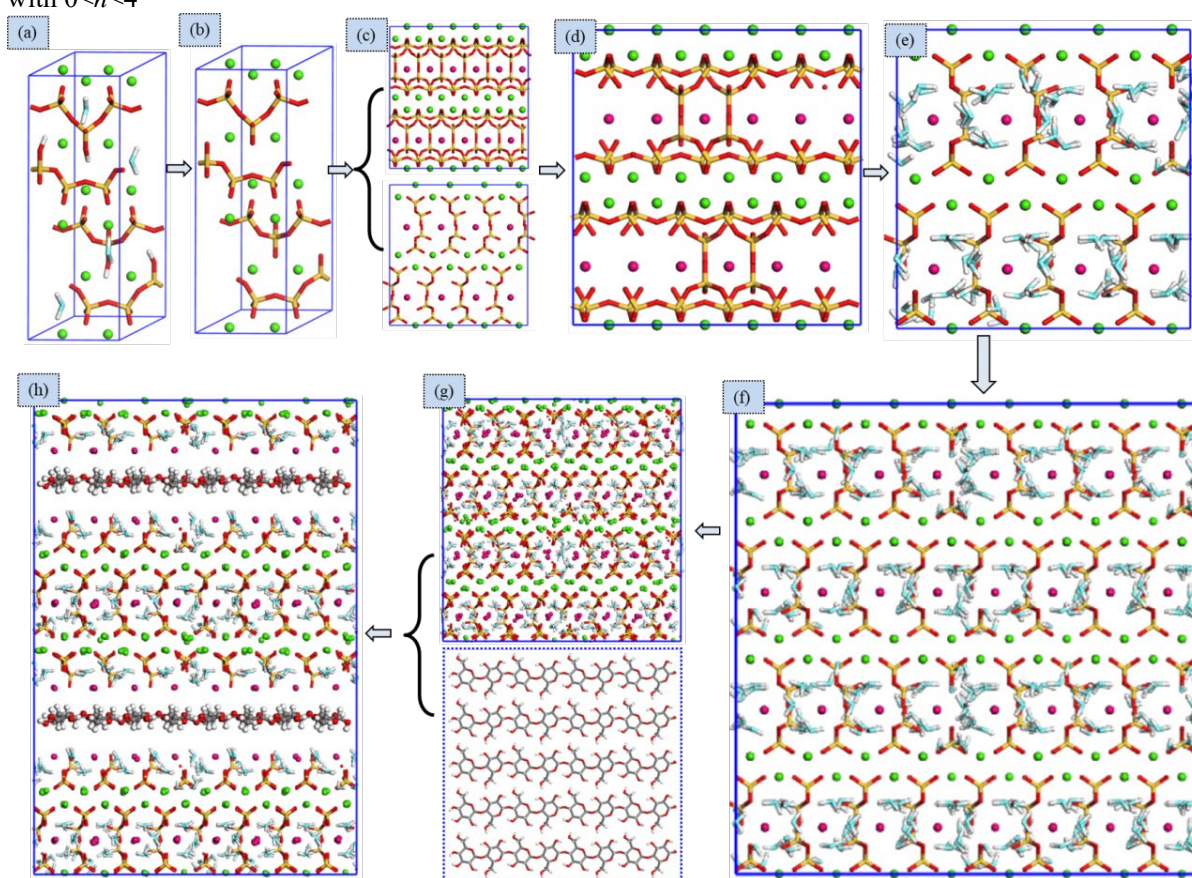


Fig. S2. Molecular model construction process of CNS. (a) Hamid tobermorite 11 Å. (b) anhydrate monoclinic structure after removal of water molecules and hydroxyl group. (c) transformation of monoclinic cell into an orthorhombic crystal structure. (d) Removal of the silicate chains to achieve different Ca/Si ratios. (e) GCMC water sorption simulation. (f) creation of supercell. (g) geometrical minimization of C-S-H cell and construction of a CNS monolayer. (h) cleavage of 001 plane with 1nm vacuum space and intercalation of CNS to establish the initial configuration of sandwich system. In the atomistic configurations, the green and purple spheres represents the inter- and intra-layer calcium atoms, red balls denote the oxygen atoms, black balls are the carbon atoms, white balls shows the hydrogen atoms, light blue-white ball stick model represents the water molecule, yellow-red bond denotes the silicate chain(Si-O), black-red-white stick model represents the CNS chain.

As strongly supported by the SEM observation as well as previous experimental evidence, the polymer chain/layer can be easily intercalated into the interlayer of C-S-H gel[11,12]. It is also the weakest region in the entire C-S-H atomic structure. The sandwich composite system is built in several steps. After initial geometrical minimization, the saturated C-S-H molecular model is cleaved at the 001 plane to create a 1.0 nm vacuum space at the inter calcium layer, which is within the typical size range of a nano-pore. The CNS monolayer is then intercalated into the vacuum space to form the sandwich system. During the construction of the nanocomposite, the length direction of the CNS chain is set as parallel to the *a*- direction of the C-S-H crystal, as shown in Fig. S2h. The final simulation box has a lattice parameter of $a=44.64 \text{ \AA}$, $b=44.34 \text{ \AA}$, $c=65.54 \text{ \AA}$, $\alpha=\beta=\gamma=90 \text{ deg}$. It is noted that according to the X-ray diffraction patterns in Fig. 2 in the main text, the presence of CNS has a broader basal reflection ($<5^\circ 2\theta$) and less intense peak than pure C-S-H that are similar to the reported literature[11–13]. By comparison with the previous experimental analysis on the XRD peak position shifting with different biomolecule concentrations, the estimated concentration of CNS in the present study is in a range between 0.09-0.18 g/g Calcium. Therefore, the constructed model having a concentration of $\approx 0.14 \text{ g/g Ca}$ salt is within the experimental range. Thereafter, the nanocomposite sandwich system is equilibrated in the isothermal-isobaric (NPT) ensemble for 100 picoseconds, thereby the cleaved vacuum space can be freely closed. As a consequence, 6 nanocomposites with realistic Ca/Si ratios based on the 6 benchmarking C-S-H models are constructed respectively, which are numbered as wh11 to wh21 for the C-S-H models, and wh11L to wh21L for C-S-H/CNS models correspondingly.

The CNS is constructed based on the chemical stoichiometry supplied by the industrial partner Cellucomp Ltd, UK. A single CNS chain has a cellulose-like crystal molecular structure that is composed of several glucose units ($\text{C}_6\text{H}_{12}\text{O}_6$). It starts out with a hexagonal ring with 5 carbons joined together by one oxygen element, known as tetrahydropyran ring. Different functional groups including the hydroxymethyl group($-\text{CH}_2\text{OH}$), hydroxyl group($-\text{OH}$) and hydrocarbon methine group($-\text{H}$) are grafted on the ring. The

glucose units are then polymerized to form a single chain. Like cellulose materials, the CNS is an allomorph, i.e. crystals in native cellulose Ia and Ib phases, regenerated II phase through mercerization, and III_I phase obtained by ammonia treatment, and anhydrous amorphous phase. In this work, the molecular structure of the CNS having a native cellulose Ia crystallographic monolayer type is constructed, which consists of 5 long chains with a degree of polymerization equal to 8 for each chain. Therefore, the computational system of the CNS contains 20 cellobiose units that are cross-linked by 40 glucoses. The corresponding molecular structure is depicted in Fig. S2g.

The bonded and non-bonded interactions in the nanocomposite system are defined by a combinational set of parameters from both the ClayFF force field[14], and the Consistent Valence Force Field(CVFF)[15]. The total potential energy is shown in Equation 1. The ClayFF force field, derived from the experimental studies and density function theory(DFT) method, is used to deal with the model of calcium silicate skeleton. This force field has already shown its robustness in modeling structures of cementitious materials[16–18]. Several previous studies on different calcium silicate systems such as tobermorite and jennite, portlandite, aluminate-ferrite monosubstituent calcium aluminum hydrate(AFm) etc., as well as modeling the sol-gel interactions between aqueous solutions and tobermorite solids have demonstrated the capability of ClayFF[19–23]. The CVFF force field is applied to address the potential states of CNS in terms of the bond stretching, angle bending and energy etc. The CVFF is chosen because of its robustness in modeling the carbohydrate molecules, and is found to be very suitable for modeling ligands, receptor proteins, cellulose and other organic compound system[15,24–26]. Particularly, it is noteworthy that the conformational behavior of methyl- α -lactoside that having a cellulose-like methyl β -1-4 linked glucopyranose unit, has been well predicted by the CVFF[24].

In the force field, the two body interactions between atoms i and j separated by a distance r_{ij} are modeled by the non-bond Lennard-Jones (12–6) potential energy function with a Coulomb pairwise term. The partial

atomic charges derived from periodic density functional theory (DFT) are used to describe the Coulombic interaction. The three-body bond interactions are defined by harmonic bond/angle style potentials, read as

$$E_{total} = E_{vdw} + E_{Coulomb} + E_{bond} + E_{angle} \quad (1)$$

where

$$\begin{cases} E_{vdw} = 4\varepsilon_{ij}[(R_{0,ij}/r_{ij})^{12} - (R_{0,ij}/r_{ij})^6] & r_{ij} < r_c \\ E_{Coulomb} = Cq_iq_j/\varepsilon_0r_{ij} & r_{ij} < r_c \\ E_{bond} = k_1(r_{ij} - r_0)^2 \\ E_{angle} = k_2(\theta_{ij} - \theta_0)^2 \end{cases} \quad (2)$$

In Equation 2, $R_{0,ij} = (R_{0,i} + R_{0,j})/2$ and $\varepsilon_{ij} = \sqrt{\varepsilon_i\varepsilon_j}$ represent the Van der Waals radius and energy well depth for the atomic pair according to the arithmetic mean rule. The coefficient $C=1/4\pi$ is energy conversion constant, and ε_0 is the dielectric permittivity of vacuum (8.85419×10^{-12} F/m). Parameters k_1 and k_2 are force constants for the bond stretching and angle bending, r_0 represents the equilibrium bond length. θ_{ij} denotes the bond angle for the metal oxygen-hydrogen, and θ_0 represents the equilibrium bond angle. The long-range Coulombic interactions were calculated by the Edwald summation method, and the r_0 cut-off distance was set as 12 Å for the pair potential describing the long range non-bonded electrostatics interactions.

For representing the water, hydroxyl and oxygen-oxygen interactions, we use the classic simple point charge (SPC) model due to its simplicity[27]. The SPC model is able to reproduce the water properties, including structural configuration, radial distribution pattern, and hydrogen bonding among water bulk. The method has been widely used in modeling the interaction of water with hydroxide mineral surfaces for the past two decades.

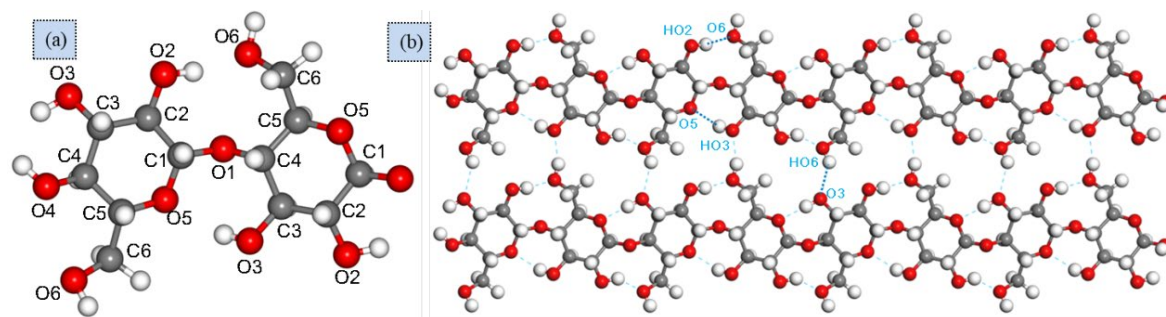


Fig. S3. Schematic diagram of the intra- and inter-molecular H bonds within the CNS. (a) numbering of different atom species. (b) H bond connections. The black, red and white sticks in the molecular model of CNS represent carbon, oxygen and hydrogen atoms, respectively.

The conformation of the CNS monolayer are stabilized by two intra-molecular hydrogen bonds, i.e. the H-bond between the oxygen in hydroxymethyl group and hydrogen in hydroxyl group ($O2-HO2...O6$), the H-bond between the hydrogen in hydroxyl group and tetrahydropyran ring oxygen ($O3-HO3...O5$), as well as the inter-molecular hydrogen bond, $O6-HO6...O3$. It is likely that having one hydrogen bond on each side of the glycosidic linkage makes the molecule more resilient to rotations, which therefore inhibits the hydroxymethyl group and the hydroxyl group to approach towards the C-S-H substrate surface. It is noted that the intra- and inter-molecular hydrogen bonds within the plane can stabilize the structure, which also contributes significantly to the stiffness of the biomaterial.

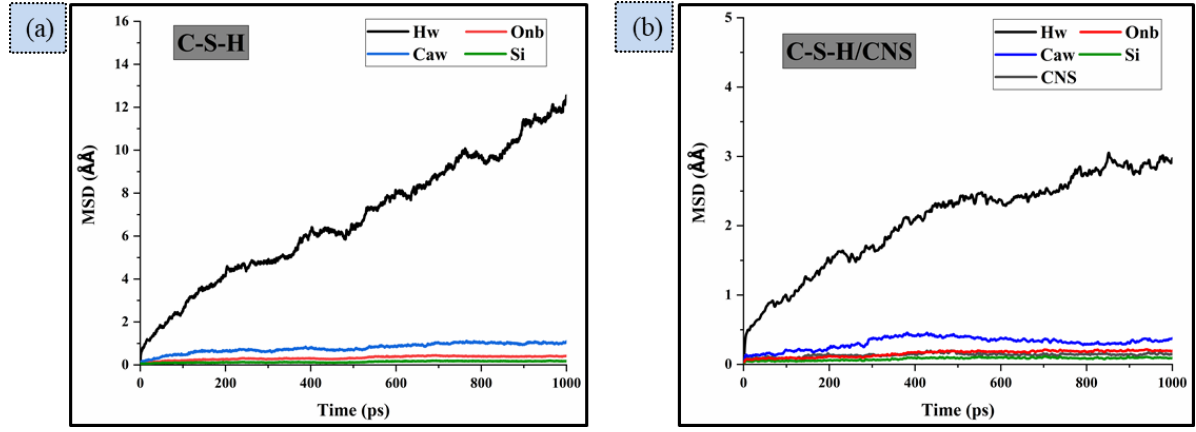


Fig. S4. MSD evolutions of different atoms in pure C-S-H and nanocomposite with Ca/Si=1.7. (a) Pure C-S-H. (b) C-S-H/CNS nanocomposite

The dynamic properties of the atoms in the C-S-H/CNS nanocomposites are characterized by the mean square displacement (MSD) defined by

$$MSD(t) = \frac{1}{n} \sum_{i=1}^n \left\langle \left| r_i(t) - r_i(0) \right|^2 \right\rangle \quad (3)$$

where the squared displacement over a group of atoms from the original position $r_i(0)$ are summed and averaged at time t . Higher MSD values indicate faster atom diffusion in the molecular system. According to the MSD curves, the atoms' mobility is ranked as: $H_2O > Caw > CNS > Si$. Silicate, oxygen and calcium atoms in both the plain C-S-H and the C-S-H/CNS nanocomposite have the MSD values below 1 \AA^2 , indicating that the calcium silicate layer acts as a skeleton in stabilizing the atomic structure. For the CNS atoms, the MSD evolution curve is similar to that of C-S-H skeleton oxygen and silica atoms due to the strong interaction with the C-S-H substrate. After ensemble equilibrium, the CNS could strongly adhere to the Onb atoms through O-Caw-O bonds. This ionic attraction limits the mobility of the CNS atoms. In the C-S-H interlayer, the Hw atoms exhibit the fastest MSD evolution, implying that water molecules are highly unstable in the C-S-H nanopore. However, in comparison to the pure C-S-H gel, the functional groups in the CNS, with strong polarity and hydrophilicity, can restrict the neighboring water molecules by the hydrogen bond, stabilizing the interlayer water. The presence of hydrophilic functional groups can effectively inhibit water movement, contributing to the cohesive strength of the composite.

Table S2. Diffusion coefficients for different atoms chunks [unit: $10^{-11}\text{m}^2/\text{s}$]

Ca/Si ratio	Model	Hw	Caw	Onb	Si	CNS
Ca/Si=1.1	C-S-H	3.5588	0.4742	0.1958	0.1109	-
	C-S-H/CNS	1.6428	0.1947	0.1119	0.0700	0.2080
Ca/Si=1.3	C-S-H	2.5924	0.3900	0.1430	0.0655	-
	C-S-H/CNS	2.1578	0.3231	0.1208	0.0951	0.1868
Ca/Si=1.5	C-S-H	2.2211	0.5412	0.2234	0.1002	-
	C-S-H/CNS	2.1514	0.3275	0.1565	0.0853	0.1389
Ca/Si=1.7	C-S-H	3.5662	0.5354	0.2134	0.0965	-
	C-S-H/CNS	2.2664	0.2483	0.1479	0.0664	0.1241
Ca/Si=1.9	C-S-H	3.9946	0.6189	0.2328	0.0911	-
	C-S-H/CNS	2.2221	0.3738	0.1550	0.0772	0.1644
Ca/Si=2.1	C-S-H	4.7577	0.6530	0.2494	0.1220	-
	C-S-H/CNS	2.2516	0.3451	0.1564	0.0752	0.1746

The diffusion coefficient D is approximated by linearly fitting the MSD curve before 200 picoseconds simulation, given as

$$D = \frac{1}{6} \frac{\partial}{\partial t} (MSD) \quad (4)$$

The D values for typical atom species in the model with different Ca/Si ratios are listed in Table S2. The computed diffusion coefficients of water hydrogen atom Hw in the pure C-S-H gel pore surface with different Ca/Si ratios range between $D=2.22 \times 10^{-11}\text{m}^2/\text{s}$ and $D=4.76 \times 10^{-11}\text{m}^2/\text{s}$, which is of the same order of the measured results from proton field cycling nuclear magnetic relaxation test ($D=3.60 \times 10^{-11}\text{m}^2/\text{s}$)[28], suggesting that the translational diffusion coefficient of water at the pore surface in hydrated cement paste is about 1/61 of bulk water. However, the D value of Hw in the C-S-H/CNS nanocomposite fluctuates around $2.2 \times 10^{-11}\text{m}^2/\text{s}$ for most cases, which is noted to be much less than that in C-S-H, indicating that the water molecules in the interlayer are strongly restrained by the CNS, and the motion of the water molecules is drastically hampered in comparison to the bulk solution in pure C-S-H gel. Since the backbone CNS chain serves as a reservoir that retains the water molecules, and the functional groups act like a root network that are deeply embedded into the bulk water and cross-linked to the neighboring silicate calcium layer, blocking the water transportation channel and inhibiting the mobility of water molecules. It is worth mentioning that the rapid movement of water at the interlayer channel can produce strong repulsive force and fluid pressure that disturb the chemical bonds in the C-S-H and weaken the connections between neighboring calcium silicate layer[29]. Therefore, one significant merit by inclusion of CNS biomaterial is to stabilize the interlayer water, reduce the flowability of the composite material and strengthen the interfacial connection. Moreover, the incorporation of the CNS can further stabilize the skeleton with smaller D values observed for silicate calcium layer atoms.

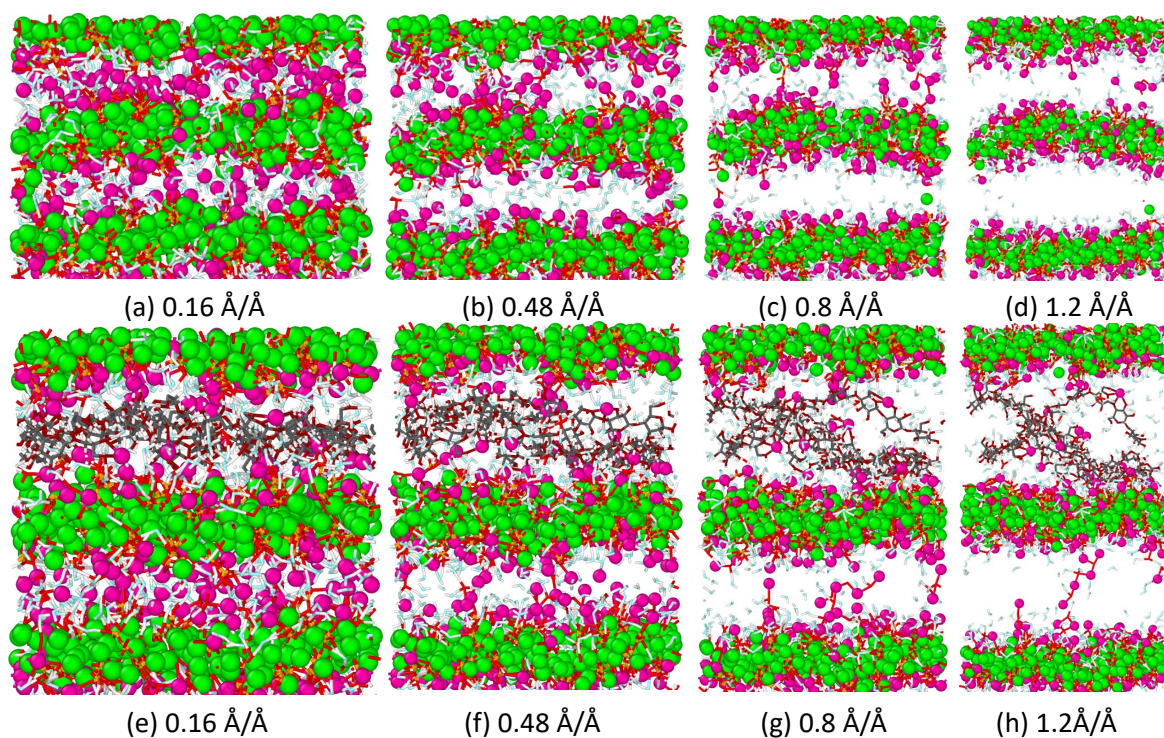


Fig. S5. Molecular structure evolution under tension in the z - direction: (a-d) plain C-S-H, (e-h) C-S-H/CNS nanocomposite. In the molecular configuration, the green and purple spheres represent the inter- and intra-layer calcium atoms, red balls denote the oxygen atoms, light blue-white ball stick model represents the water molecule, yellow-red bond denotes the silicate chain (Si-O), black-red-white stick model represents the CNS chain.

When the models are tensioned along the z - direction, the crack in the plain C-S-H model nucleates at the weakest interlayer region. The ionic bonds between Caw and O are the main source bearing the tensile loading, as shown in Fig. S5a-d. The interfacial Caw-O and hydrogen bonds are stretched and start to break at a strain level of 0.2 \AA^{-1} . Thereafter, the crack gradually opens up until fractured apart with a major gap occurred between the neighboring silicate layers. However, for the nanocomposite model, the hexagon structure in the CNS monolayer is highly deformed and distorted along the z - direction. A few functional groups at the two ends of the CNS chain are deeply rooted at the interlayer region, postponing the fracture by linking the opening crack between the neighboring calcium silicate layers, therefore retarding the crack growth and preventing the abrupt rupture. However, the eventual failure of the nanocomposite is still originated from the weakest interlayer region where the CNS is absent (see Fig. S5e-h). This phenomenon suggests that a higher mechanical performance of the nanocomposite in the z - direction can be possibly achieved by inclusion of more biomaterial with higher volume fraction, as the possibility of the CNS intercalation at the interlayer region can be increased.

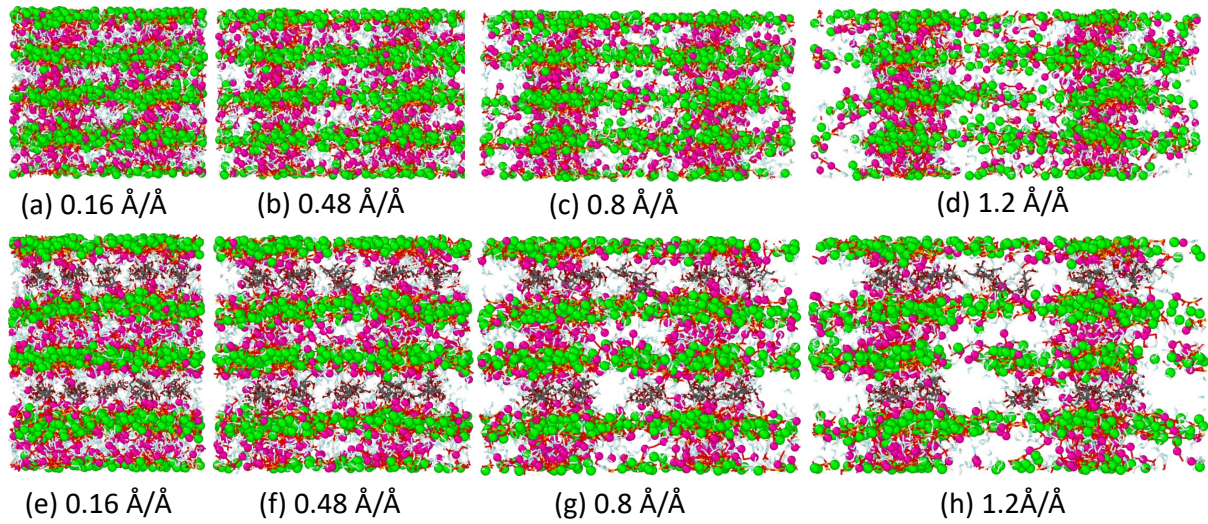


Fig. S6. Molecular structure evolution under tension in the y - direction: (a-d) pure C-S-H, (e-h) C-S-H/CNS nanocomposite. In the molecular configuration, the green and purple spheres represent the inter- and intra-layer calcium atoms, red balls denote the oxygen atoms, light blue-white ball stick model represents the water molecule, yellow-red bond denotes the silicate chain (Si-O), black-red-white stick model represents the CNS chain.

As deformed in the y - direction, a stable covalent Si–O–Si bond is stretched longer in the C-S-H model, and the ionic bonds between the Ca and Si–O groups are elongated until broken. It is not surprising that the macro crack is generated at the initial defects of the silicate chain preceding to the fracture. With respect to the C-S-H/CNS nanocomposite, the reinforcing effect of the CNS is only valid at the pre-peak region, since the inter-molecular H bond connections (O2–HO2...O6) between the adjacent chains can be easily ruptured at a small deformation, as shown in Fig. S6. When the strain level increases from 0.16 to 0.48 $\text{\AA}/\text{\AA}$, the adjacent CNS chains are detached at the location of cracking. Thereafter, with further crack propagation, the H bond connections between the neighboring chains are completely missing, and the CNS sheet geometry is disturbed with the water molecules and calcium atoms agglomerated around the chains, which explains the nanocomposite has similar post-peak performance with the neat C-S-H gel but higher stiffness and strength at pre-peak region.

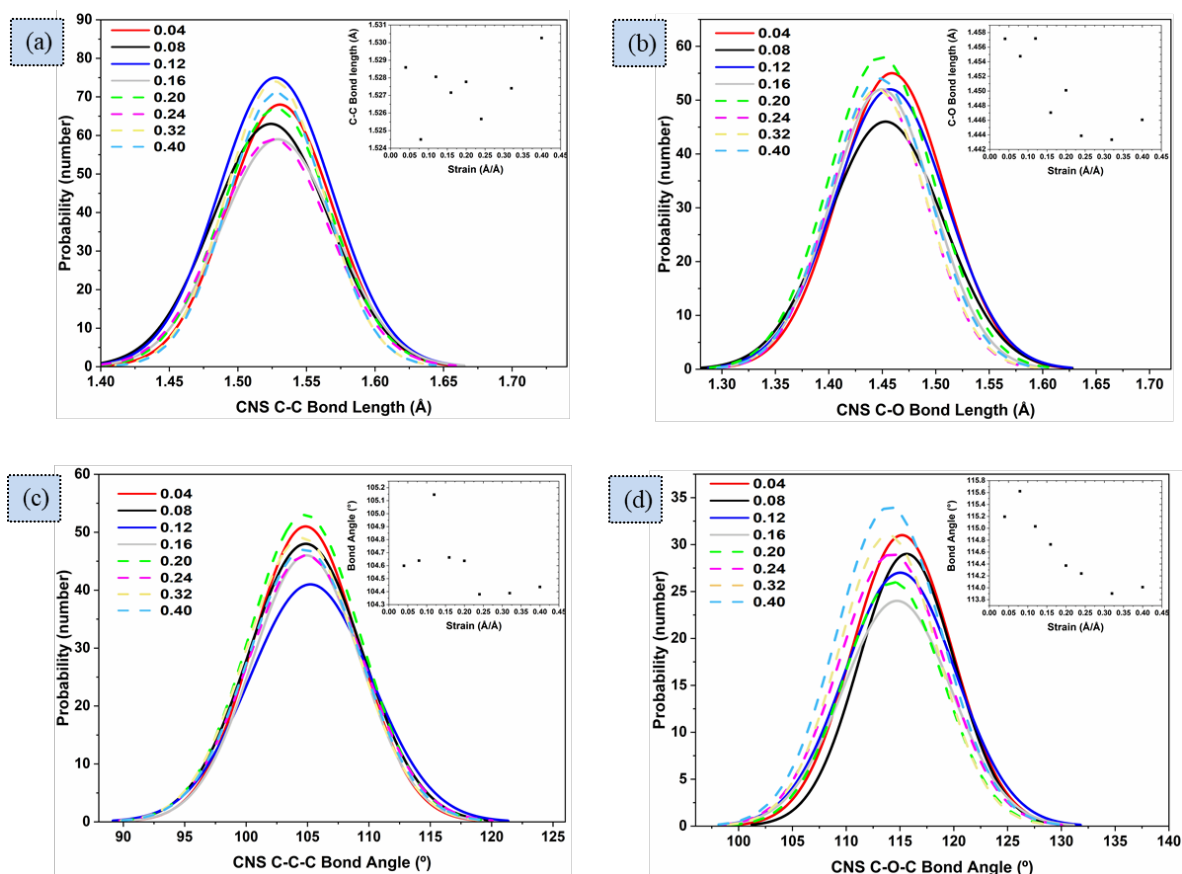


Fig. S7. BLE and BAD of CNS chain in the y - direction. (a) BLE of C-C bond. (b) BLE of C-O bond. (c) BAD of C-C-C angle. (d) BAD of C-O-C angle.

In the y - direction, the BLE and BAD for C-C and C-O bond are illustrated in Fig. S7. The variation of BLE and BAD is much less in comparison to the x - direction, with certain fluctuations of the count number evolution observed during the tensile loading. The C-C bond length remains in the range of 1.525 Å-1.53 Å with indiscernible change in the C-C-C angle distribution (from 90 to 120 deg), the change in the mean bond angle is also within one degree (from 104.3-105.2 deg), less than the case in the x - direction. In addition, the C-O bond length is slightly reduced from 1.458 to 1.443 deg, together with the C-O-C bond angle decreasing from 115.6 to 113.8 deg. The decrease in the BLE is largely due to the Poisson's effect that the composite sample undergoes “shrink” along the x - direction, which can help to release the tensile stress within the C-C bond. While the reduction in the bond angle is also partially attributed to the elongation of Oc-Caw-Oh bond in the y - direction, during the loading process, the glycosidic linkage oxygen is dragged along the y - direction, leading to the folding of the C-O-C bond angle.

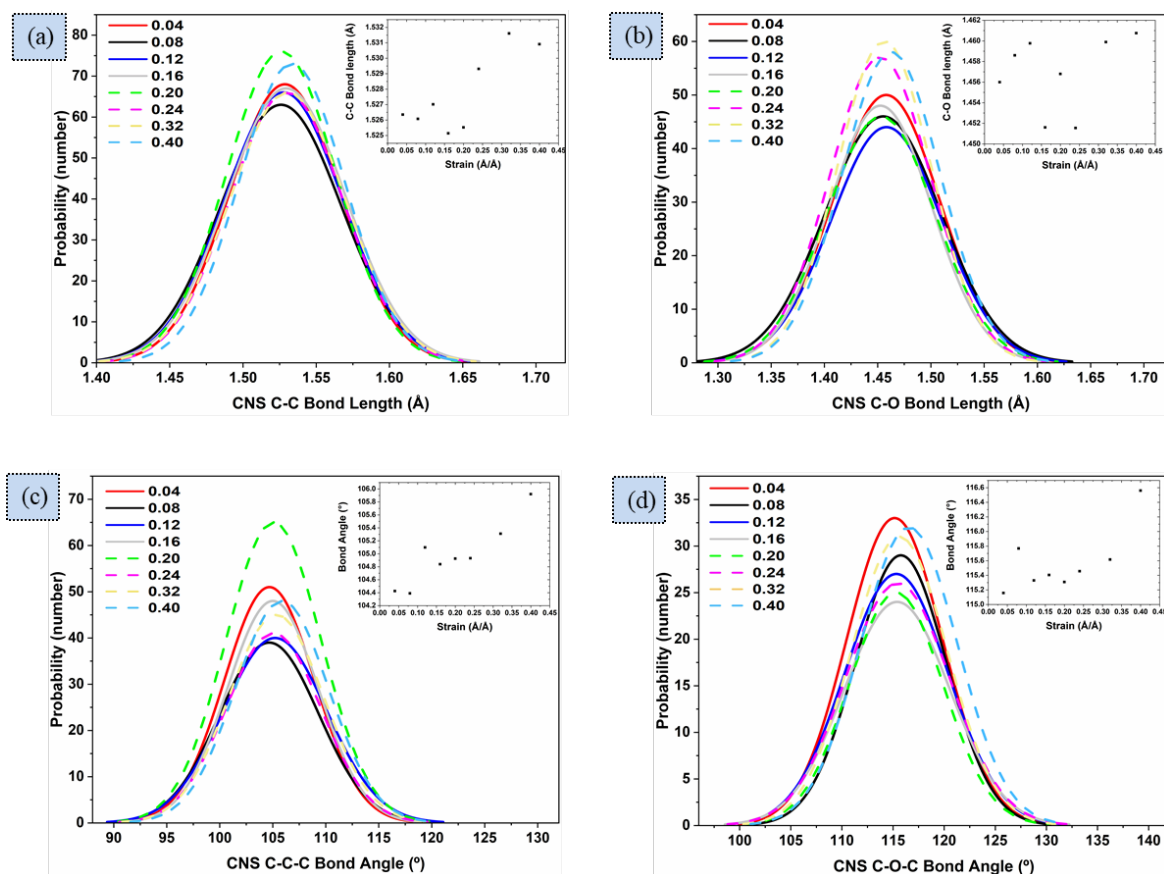


Fig. S8. BLE and BAD CNS chain in the z - direction. (a) BLE of C-C bond. (b) BLE of C-O bond. (c) BAD of C-C-C angle. (d) BAD of C-O-C angle.

In contrary to the y - direction, an overall increase in the mean bond angle and the bond length values is observed for both the C-C and C-O bonds in the z - direction, notwithstanding that a more random evolution process of the BLE and BAD is found during the deformation process, as shown in Fig. S8. Since the CNS chain is mainly connected to the calcium silicate layer through the functional groups during the loading, the chain is gradually aligned along the z - direction due to its flexibility. Therefore, the C-C mean bond length still lies in a small range between 1.525 Å to 1.532 Å, with a C-C-C mean bond angle increase from 104.3 to 106.0 deg. It is also reasonable that a similar trend is observed for the C-O bond with the bond length varying from 1.45 Å to 1.46 Å, and the C-O-C angle increases from 115.1 to 116.6 deg.

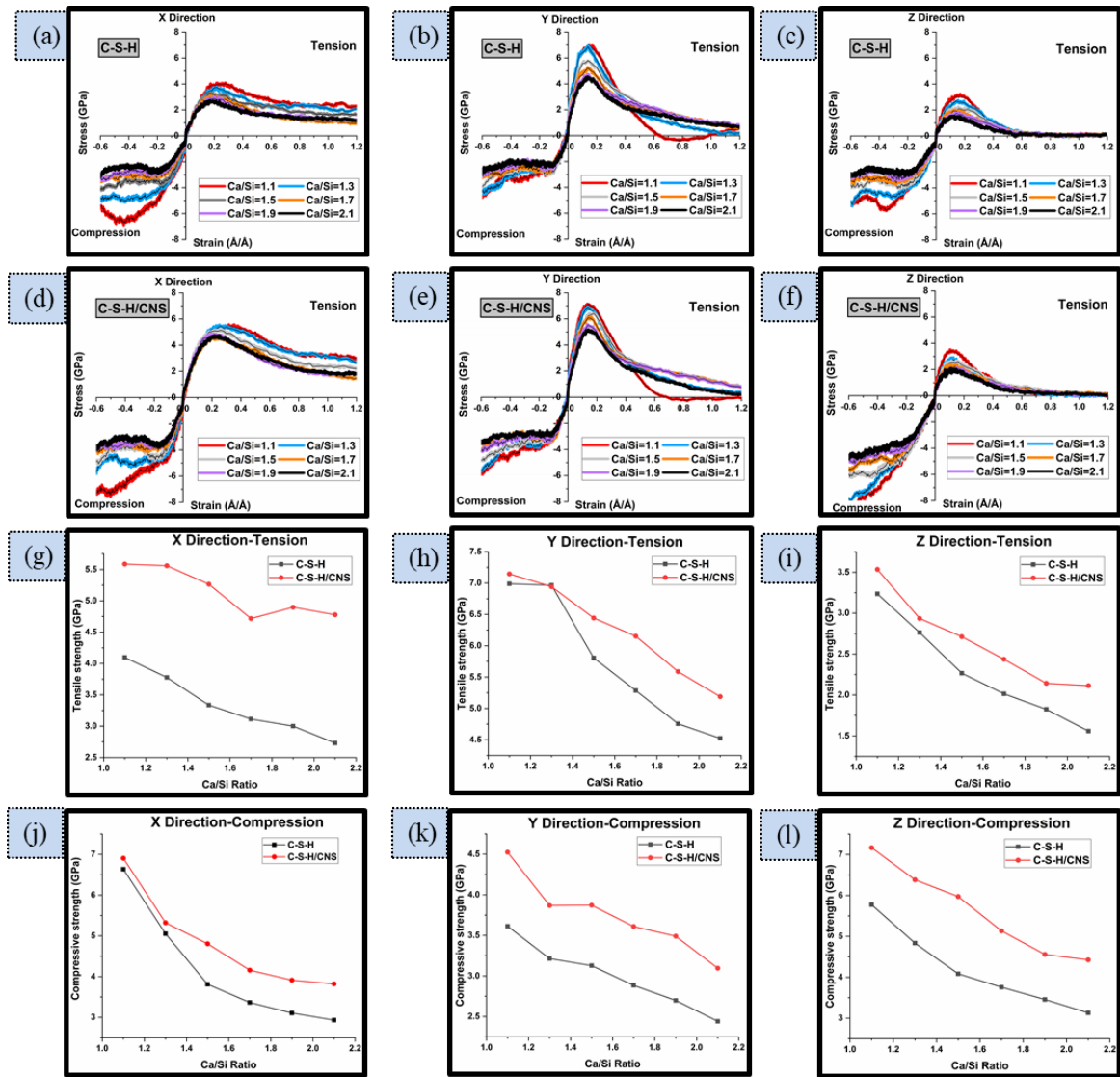


Fig. S9. Constitutive behavior of the C-S-H and nanocomposite samples for various Ca/Si ratios at the three directions under tension and compression. (a-c) stress-strain curves for pure C-S-H. (d-f) stress-strain curves for C-S-H/CNS nanocomposite. (g-i) Variation of tensile strengths with increasing Ca/Si ratio. (j-l) Variation of compressive strengths with increasing Ca/Si ratio.

It is noticed that there is a strain-hardening effect for low Ca/Si ratio especially for the nanocomposite samples. In order to evaluate the percentage of increase, the corresponding compressive strength is then defined as the maximum stress before a strain level of 0.4 for reasonable comparisons, as the peak strength usually appears before this strain level for pure C-S-H samples.

As shown in Fig. S9, the tensile stress-strain curves for both the pure C-S-H and the nanocomposites undergo three stages in all the three directions: (I) the elastic stage, proportional increase in the stress with a strain increment is observed until about 30% of the peak stress, (II) the yield stage, where the stress-strain relation becomes nonlinear until the stress reaches its peak value, (III) the strain softening stage, the stress

starts to gradually decrease with strain increment. When the models are loaded in the z - direction, the tensile strength of the plain C-S-H model reduces from 3.237GPa to 1.559GPa with an increase in Ca/Si ratio from 1.1 to 2.1, while the tensile strength of the nanocomposite model also shows a decreasing trend from 3.535 GPa to 2.114 GPa. The decrease in the tensile strength is also true for the x - and the y - directions as the Ca/Si ratio is increasing.

The nanocomposite also shows favorable increase in the compressive strength in comparison to the pure C-S-H. The stress-strain curves of the nanocomposite can be divided into three stages during the compressive loading: (I) the elastic stage: the stress linearly increases with increasing the strain up to about 0.1 Å for all the three directions. The incorporation of CNS significantly strengthens the initial stiffness and increase the slope particularly for high Ca/Si ratios; (II) The elasto-plastic stage: the stress slowly rises with increasing the strain, where the initial turning point(yield strength) becomes vague in the z - direction, (III) the strain hardening stage: the stress continuously increases with an increase in strain due to the persistent lateral confinement effect of the CNS and the strain hardening phenomenon with improved ductility is rather obvious, especially in the z - direction. However, the cases in the x - and the y - directions with Ca/Si ratio larger than 1.5 demonstrate slight strain softening behavior followed by a plateau, as the confinement effect from the CNS is not significant. The behavior is thus similar to the pure C-S-H for different Ca/Si ratios. In the x - direction, the strength increasing ratios start from approximate 4% to 30% with various Ca/Si ratios. A more stable increase in the y - direction is observed around 25% for all the cases, while much higher increase ratios ranged between 24% and 46% are obtained in the z - direction. Furthermore, stronger strain-hardening of the nanocomposite is noted, in particular for the cases with relative low Ca/Si of 1.1 and 1.3, suggesting that the inclusion of CNS can be very effective in either increasing the compressive ductility for lower Ca/Si ratios or improving the compressive strength for higher Ca/Si ratios.

Table S3. Summary of the strengths of C-S-H and nanocomposite in tension and compression

Tensile strength (GPa)									
Ca/Si ratio	Pure C-S-H			C-S-H/CNS					
	<i>x</i>	<i>y</i>	<i>z</i>	<i>x</i>	Increase ratio[%]	<i>y</i>	Increase ratio[%]	<i>z</i>	Increase ratio[%]
1.1	4.097	6.987	3.237	5.585	36.32	7.146	2.28	3.535	9.21
1.3	3.777	6.964	2.763	5.559	47.18	6.942	-0.32	2.935	6.23
1.5	3.336	5.806	2.266	5.264	57.79	6.443	10.97	2.712	19.68
1.7	3.113	5.285	2.014	4.716	51.49	6.151	16.39	2.436	20.95
1.9	3.000	4.755	1.825	4.897	63.23	5.587	17.50	2.143	17.42
2.1	2.73	4.523	1.559	4.777	74.98	5.188	14.70	2.114	35.60
Compressive strength (GPa)									
Ca/Si ratio	Pure C-S-H			C-S-H/CNS					
	<i>x</i>	<i>y</i>	<i>z</i>	<i>x</i>	Increase ratio[%]	<i>y</i>	Increase ratio[%]	<i>z</i>	Increase ratio[%]
1.1	6.635	3.6125	5.773	6.904	4.05	4.5241	25.23	7.166	24.13
1.3	5.052	3.21355	4.835	5.323	5.36	3.86778	20.36	6.382	32.00
1.5	3.811	3.12686	4.085	4.806	26.11	3.87147	23.81	5.974	46.24
1.7	3.366	2.88378	3.757	4.158	23.53	3.60961	25.17	5.133	36.62
1.9	3.106	2.6985	3.456	3.914	26.01	3.4896	29.32	4.559	31.92
2.1	2.931	2.44134	3.129	3.821	30.37	3.09553	26.80	4.425	41.42

Reference

- [1] Richardson IG, Groves GW. Microstructure and microanalysis of hardened ordinary Portland cement pastes. *J Mater Sci* 1993;28:265–77.
- [2] Blanc P, Bourbon X, Lassin A, Gaucher EC. Chemical model for cement-based materials: Temperature dependence of thermodynamic functions for nanocrystalline and crystalline C–S–H phases. *Cem Concr Res* 2010;40:851–66.
- [3] Hamid SA. The crystal structure of the 11Å natural tobermorite. *Zeitschrift Fur Krist* 1981;8:1–10.
- [4] Merlino S, Bonaccorsi E, Armbruster T. The real structure of tobermorite 11A: normal and anomalous forms, OD character and polytypic modifications. *Eur J Mineral* 2001;13:577–90. <https://doi.org/10.1127/0935-1221/2001/0013-0577>.
- [5] Pellenq RJ-M, Kushima A, Shahsavari R, Van Vliet KJ, Buehler MJ, Yip S, et al. A realistic molecular model of cement hydrates. *Proc Natl Acad Sci* 2009;106:16102–7.
- [6] Cong X, Kirkpatrick RJ. 29Si MAS NMR study of the structure of calcium silicate hydrate. *Adv Cem Based Mater* 2002;3:144–56. [https://doi.org/10.1016/s1065-7355\(96\)90046-2](https://doi.org/10.1016/s1065-7355(96)90046-2).
- [7] Qomi MJA, Krakowiak KJ, Bauchy M, Stewart KL, Shahsavari R, Jagannathan D, et al. Combinatorial molecular optimization of cement hydrates. *Nat Commun* 2014;5:4960.
- [8] Frenkel D, Smit B. Understanding molecular simulation: From algorithms to applications. *Comput Sci Ser* 2002;1:1–638.
- [9] Hou D, Ma H, Zhu Y, Li Z. Calcium silicate hydrate from dry to saturated state: Structure, dynamics and mechanical properties. *Acta Mater* 2014;67:81–94. <https://doi.org/10.1016/j.actamat.2013.12.016>.
- [10] Chen JJ, Thomas JJ, Taylor HFW, Jennings HM. Solubility and structure of calcium silicate hydrate. *Cem Concr Res* 2004;34:1499–519. <https://doi.org/10.1016/j.cemconres.2004.04.034>.
- [11] Matsuyama H, Young JF. Intercalation of Polymers in Calcium Silicate Hydrate: A New Synthetic Approach to Biocomposites? *Chem Mater* 2002;11:16–9. <https://doi.org/10.1021/cm980549l>.
- [12] Matsuyama H, Young JF. Synthesis of calcium silicate hydrate/polymer complexes: Part I. Anionic and nonionic polymers. *J Mater Res* 1999;14:3379–88.
- [13] Kamali M, Ghahremaninezhad A. Effect of Biomolecules on the Nanostructure and Nanomechanical Property of Calcium-Silicate-Hydrate. *Sci Rep* 2018;8:1–16. <https://doi.org/10.1038/s41598-018-27746-x>.
- [14] Cygan RT, Liang J-J, Kalinichev AG. Molecular Models of Hydroxide, Oxyhydroxide, and Clay Phases and the Development of a General Force Field. *J Phys Chem B* 2004;108:1255–66. <https://doi.org/10.1021/jp0363287>.
- [15] Gaedt K, Hölting H. Consistent valence force-field parameterization of bond lengths and angles with quantum chemical ab initio methods applied to some heterocyclic dopamine D3-receptor agonists. *J Comput Chem* 1998;19:935–46.
- [16] Cygan RT, Greathouse JA, Heinz H, Kalinichev AG. Molecular models and simulations of layered materials. *J Mater Chem* 2009;19:2470–81. <https://doi.org/10.1039/b819076c>.
- [17] Kalinichev AG, Wang J, Kirkpatrick RJ. Molecular dynamics modeling of the structure, dynamics and energetics of mineral-water interfaces: Application to cement materials. *Cem Concr Res* 2007;37:337–47. <https://doi.org/10.1016/j.cemconres.2006.07.004>.

- [18] Kalinichev AG, Kirkpatrick RJ. Molecular dynamics modeling of chloride binding to the surfaces of calcium hydroxide, hydrated calcium aluminate, and calcium silicate phases. *Chem Mater* 2002;14:3539–49.
- [19] Hou D, Li T. Influence of aluminates on the structure and dynamics of water and ions in the nanometer channel of calcium silicate hydrate (C–S–H) gel. *Phys Chem Chem Phys* 2018;20:2373–87.
- [20] Ding Q, Yang J, Hou D, Zhang G. Insight on the mechanism of sulfate attacking on the cement paste with granulated blast furnace slag: An experimental and molecular dynamics study. *Constr Build Mater* 2018;169:601–11.
- [21] Yang J, Hou D, Ding Q. Ionic hydration structure, dynamics and adsorption mechanism of sulfate and sodium ions in the surface of calcium silicate hydrate gel: A molecular dynamics study. *Appl Surf Sci* 2018;448:559–70.
- [22] Wang L, Hou D, Shang H, Zhao T. Molecular dynamics study on the Tri-calcium silicate hydration in sodium sulfate solution: Interface structure, dynamics and dissolution mechanism. *Constr Build Mater* 2018;170:402–17.
- [23] Hou D, Li D, Yu J, Zhang P. Insights on capillary adsorption of aqueous sodium chloride solution in the nanometer calcium silicate channel: a molecular dynamics study. *J Phys Chem C* 2017;121:13786–97.
- [24] Asensio JL, Martin-Pastor M, Jimenez-Barbero J. The use of CVFF and CFF91 force fields in conformational analysis of carbohydrate molecules. Comparison with AMBER molecular mechanics and dynamics calculations for methyl α -lactoside. *Int J Biol Macromol* 1995;17:137–48.
- [25] Dauber-Osguthorpe P, Roberts VA, Osguthorpe DJ, Wolff J, Genest M, Hagler AT. Structure and energetics of ligand binding to proteins: Escherichia coli dihydrofolate reductase-trimethoprim, a drug-receptor system. *Proteins Struct Funct Bioinforma* 1988;4:31–47.
- [26] Hardy BJ, Sarko A. Conformational analysis and molecular dynamics simulation of cellobiose and larger celooligomers. *J Comput Chem* 1993;14:831–47.
- [27] Berendsen HJC, Grigera JR, Straatsma TP. The missing term in effective pair potentials. *J Phys Chem* 1987;91:6269–71.
- [28] Korb J-P, Monteilhet L, McDonald PJ, Mitchell J. Microstructure and texture of hydrated cement-based materials: A proton field cycling relaxometry approach. *Cem Concr Res* 2007;37:295–302.
- [29] Bonnaud PA, Ji Q, Coasne B, Pellenq R-M, Van Vliet KJ. Thermodynamics of water confined in porous calcium-silicate-hydrates. *Langmuir* 2012;28:11422–32.